Phase field simulation of early-age fracture in cement-based materials

Thanh-Tung Nguyen[a,], Danièle Waldmann[a], Tinh Quoc Bui[b]

[a] *University of Luxembourg, Laboratory of Solid Structures,*
6, Avenue de la Fonte, L-4364, Esch-sur-Alzette, Luxembourg
[b] *Tokyo Institute of Technology, Department of Civil and Environmental Engineering,*
2-12- 1-W8- 22, Ookayama, Meguro-ku, Tokyo 152-8552, Japan.

Abstract

In this paper, a new computational approach, which is based on a multi-physics coupling of the chemo-thermo-mechanical process, is developed for modeling failure mechanism in cement-based materials at early-age hydration. A new constitutive law describing mechanical behavior of young concrete is thus derived, taking into account the effects of several factors including thermal expansion, shrinkage, damage, and both basic and transient thermal creeps. A strongly coupled model describing the interaction between fracture and multi-physics problems of cement hydration is obtained. The present phase field model in terms of smeared crack approach is highly suitable for simulating crack, especially when considering the unilateral contact conditions at crack surfaces. The capability of the proposed model in modeling complex crack initiation and propagation under arbitrary boundary conditions is highlighted. Fracture phenomena at both macroscopic and mesoscopic scales are considered and analyzed. The effects of creep and microstructural heterogeneity in different length scale are investigated, showing the great potential of the developed approach.

Keywords: Multi-Physics, Phase field model, Creep, Complex crack networks, Early-age concrete, Thermal variations, Shrinkage

---

1. Introduction

Early-age mechanical and thermal properties of cement-based materials in the hydration process present a significant risk for cracking, having a major impact on the lifespan of structures. Since the change of mechanical property is fast and largely dependent on the chemical and physical processes, thus modeling of early-age fracture in such cement-based materials by means of numerical approaches is not a trivial task. It often requires solving a so-called multi-physics problem of hydration process including many aspects such as chemical, thermal, mechanical, environmental, creep and shrinkage

---

Email address: `thanh-tung.nguyen@uni.lu` (Thanh-Tung Nguyen)

effects [1, 2]. The preceding studies on this area have shown that fracture of the young cement-based material strongly depends on creep effects, in particular, basic and transient thermal creeps. According to the most cited mechanisms in literature, these two creep phenomena are due to the water micro-diffusion [3, 4] and viscous shear of C-S-H [5, 6]. As a consequence, the prediction of early-age crack initiation and propagation using numerical simulation, from microscopic to macroscopic scales, is an extremely complicated problem, remaining a challenging and largely open issue.

Many numerical models developed for evaluating the risk of cracking in young concrete have been introduced in the literature. For instance, de Borst and Van den Boogaard [7] proposed a computational approach for fracture assessment at the structural level. The coupled thermo-chemo-mechanical framework for estimating the material performance and the risk of cracking due to cement hydration has been established by Cervera et al. [8, 9]. Yuan and Wan [10] developed a theoretical procedure based on the characteristics of concrete for simulating the whole hydration process after concrete setting. Thermal cracking induced by the hardening process of massive concrete elements studied by a numerical model based on the degree of hydration is reported by De Schutter [11]. Bažant et al. [12] introduced an interesting approach within the framework of crack band model, where the influences of creeps, aging and temperature are all included. In the same context, a finite element based model is presented in [13] to predict early-age cracking, where all the effects of thermal transfer, hydration, subsequent release of heat, autogenous/thermal shrinkage and creep are taken into account. The fracture of young massive concrete structures is studied in [14] by using a hydration based microplane model, and in [15] by a model employing the Mazars's damage criterion [16, 17]. In [18], the microcracking induced by differential drying shrinkage is investigated, wherein the cracking is simultaneously evaluated by both isotropic elastic damage model [16] and orthotropic elasticplastic-damage model [19]. A significant contribution considering the role of early-age basic creep is presented in [6] with an approach that combines both experimental and numerical techniques. The microstructural effects are only considered in a few studies such as the effects of aggregate size and volume fraction [20], and the impacts of structural topology, reinforcement, and concrete composition [21], or the influences of microstructural heterogeneity in our previous study employing a new computational chemo-thermo-mechanical coupling phase-field model, but without considering the creep effect [22]. Curious readers may also refer to other contributions, e.g., see Refs. [23–28]. However, one major limitation in those studies lies in the fact that the cracking phenomenon is often investigated by simplified models, for which the interaction among fracture and other aspects such as hydration, thermal transfer, and creep is usually not taken into consideration. An effective computational approach that is able to accurately predict the behavior of young concrete from microscopic scale to macroscopic scale by fully coupling multi-physics process and damage is still missing.

The main objective of this contribution is to develop an effective computational approach based on phase field model, which is substantially extended from our works in [22], for accurately evaluating the early-age cracking behavior of the cement-based material. The key novel aspect is devoted to an efficient scheme that accounts for the effects of both basic and transient thermal creeps. It should be noticed here that the developed computational model now takes into account all expected relevant phenomena that occur at early-age in autogeneous conditions, for instance, heat transfer, hydration, autogenous/thermal shrinkage, damage, and creeps. More specifically, the basic and transient thermal creeps are modeled following the works [13, 29], and incorporated into the proposed formulation in [22]. A new constitutive law considering the mechanical behavior of young concrete is derived, where the mechanical problem can be directly solved from the stress equilibrium equation at an investigated time (instead of incremental stress as proposed in the literature works [13, 15, 19]).

The present scheme allows us to describe the interactions of damage with multi-physics processes of hydration more accurately. The analysis of the crack development is later performed with a versatile phase field model in the framework of smeared crack models, which is introduced by Marigo and Francfort [30]. This method makes use of a regularized description of discontinuities through an additional phase field variable and strongly alleviates meshing problems by describing brittle cracking. Phenomena of nucleation, interaction and arbitrary crack morphologies can thus be handled in an efficient way. The detail of this approach can be found in, e.g., Refs. [31–35]. It is worth mentioning that the developed model is able to handle complex fracture at different scales thanks to the gradient-type damage conception of the phase field model [36]. Extremely complex fracture phenomena at micro/mesoscopic scales can thus be modeled by the present approach, by accounting for the microstructural details of cement-based materials. However, it should be noticed that the drying shrinkage is not considered here. This means that the early-age behavior in thin structures, where the effects of thermal strain and autogenous shrinkage are not significantly dominant compared to the drying shrinkage, is not investigated in the present work. In addition, the concrete mixture with a high water/cement ratio is also not considered in this analysis due to the fact that it is strongly affected by the drying process.

The paper is structured as follows. In Section 2, a brief description of the mathematical model for the proposed approach is given, and a short review about the chemo-thermal model to evaluate the heat of hydration and the material hardening effect is presented. In the same section, the new phase field method for modeling complex crack propagation due to thermal, shrinkage and creep strains are also derived. In Section 3, the applicability, accuracy, and performance of the developed approach are demonstrated through several numerical examples involving early-age crack onset and propagation at different scales. Some major conclusions are finally given.

2. Description of mathematical model

Let $\Omega \subset \mathbb{R}^D$ be an open domain describing a hydration system at time t, containing a crack, with D being the space dimension and $\partial\Omega$ its boundary, as depicted in Fig. 1. Following our previous study [22], the state of system is defined by four state variables, *i.e.*, temperature $T(\mathbf{x})$, displacement $\mathbf{u}(\mathbf{x})$, hydration degree $\alpha(\mathbf{x})$, and phase field $d(\mathbf{x})$. Herein, the phase field $d(\mathbf{x})$ is employed to describe the damage/fracture level, with $d(\mathbf{x}) = 0$ for intact material and $d(\mathbf{x}) = 1$ for fully damaged material. The fracture surface can be then approximated by a smeared surface, defined as

$$\Gamma_\ell(d) = \int_\Omega \gamma(d, \nabla d)\ \mathrm{d}\Omega, \quad \text{with} \quad \gamma(d, \nabla d) = \frac{1}{2\ell} d^2 + \frac{\ell}{2} \nabla d \cdot \nabla d. \tag{1}$$

In Eq. (1), $\gamma(d, \nabla d)$ is the crack density function per unit volume [31, 33, 34]; ℓ is a regularization parameter which controls the size of the diffused zone. As discussed in the literature, see e.g., [35, 37, 38], the parameter ℓ also affects the critical stress of crack initiation. The choice of ℓ in a specific application is clarified in Appendix A.

The proposed model will incorporate four main processes of cement hydration at early ages: thermal transfer, hydration, fracture, and mechanical problem. The influence of moisture diffusion is not considered here, as it often plays an important role in the thicker bodies. However, in the thinner systems, the characteristic time of this process is much slower compared to the one of heat transfer. Hence, we neglect the effect of moisture diffusion [12] in such system.

2.1. Energetic response function

Free energy of the investigated system, which is assumed to be a function of the primary variables $\{\boldsymbol{\varepsilon}^e, \alpha, T, d, \nabla d\}$, can be split into three main parts including the elastic stored energy, the fracture surface energy, and the thermo-chemical energy. In terms of regularized framework, it can be expressed as follows:

$$E(\boldsymbol{\varepsilon}^e, d, \alpha, T) = \int_\Omega \psi^e\big(\boldsymbol{\varepsilon}^e, d\big)\ \mathrm{d}\Omega + \int_\Omega \psi^d(d, \nabla d)\ \mathrm{d}\Omega\ + \int_\Omega \psi^{T\alpha}(T, \alpha)\ \mathrm{d}\Omega, \tag{2}$$

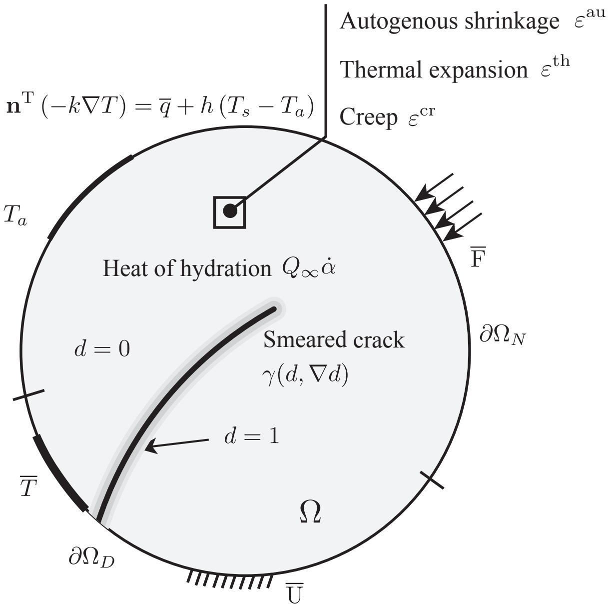

Figure 1: Schematic representation of the investigated system: a solid body containing a crack, in which the hydration reaction takes place during the hardening process.

where ε^e is the elastic strain tensor; ψ^e is the density of the elastic energy; ψ^d is the density of fracture energy; and $\psi^{T\alpha}(T,\alpha)$ describes the thermo-chemical contributions to the stored energy per unit volume.

The explicit formulation for each part of the energy density is detailed as follows. The density of elastic energy ψ^e is

$$\psi^e=\frac{1}{2}\Big[\boldsymbol{\varepsilon}^e\colon\mathbb{C}(d)\colon\boldsymbol{\varepsilon}^e\Big],\tag{3}$$

with $\mathbb{C}(d)$ being the elastic stiffness tensor accounted for damage. The density of fracture energy ψ^d describes an amount of energy released upon the creation of a new fracture surface is defined as

$$\psi^d=g_c(\alpha)\gamma(d,\nabla d),\tag{4}$$

in which, $g_c(\alpha)$ represents the fracture resistance of material at the hydration degree α. This issue will be further clarified in subsection 2.3.2.

The density of thermo-chemical energy $\psi^{T\alpha}(T,\alpha)$ is chosen, according to Cervera et al. [8], as

$$\psi^{T\alpha}=-\frac{\rho c}{2T_0}(T-T_0)^2+\frac{Q_\infty\alpha}{T_0}(T-T_0)+h(\alpha),\tag{5}$$

where ρc is the volumetric heat capacity; T_0 is the initial temperature; $Q_\infty \alpha$ describes the released heat due to hydration reaction, with Q_∞ being the total potential heat; and $h(\alpha)$ is the chemical contribution [1, 8].

The free energy can be rewritten as $E = \int_\Omega \psi \, \mathrm{d}\Omega$, in which ψ is identified as the total free density energy

$$\psi = \psi^e + \psi^d + \psi^{T\alpha}. \tag{6}$$

2.2. Thermodynamics

Without external micro forces, the Clausius-Duhem inequality can be written as follows:

$$\mathcal{D} = \boldsymbol{\sigma} \colon \dot{\boldsymbol{\varepsilon}}^e - \dot{\psi} - S\dot{T} - \boldsymbol{q} \cdot \frac{\nabla T}{T} \geq 0, \tag{7}$$

where $\boldsymbol{\sigma}$ is the stress tensor; S, $\boldsymbol{q}$ are the entropy density and the heat flux, respectively.

Using the definition of free energy density ψ in Eq. (6), the local dissipation Eq. (7) can be rewritten as

$$\mathcal{D} = \left(\boldsymbol{\sigma} - \frac{\partial \psi}{\partial \boldsymbol{\varepsilon}^e}\right) \colon \dot{\boldsymbol{\varepsilon}}^e - \left(\frac{\partial \psi}{\partial T} + S\right)\dot{T} + \mathcal{A}_d \dot{d} + \mathcal{A}_\alpha \dot{\alpha} - \boldsymbol{q} \cdot \frac{\nabla T}{T} \geq 0, \tag{8}$$

where $\mathcal{A}_d = -\frac{\delta \psi}{\delta d} = -\frac{\partial \psi}{\partial d} + \nabla . \left(\frac{\partial \psi}{\partial \nabla d}\right)$ is the variational derivative of ψ with respect to the phase field d; The chemical affinity $\mathcal{A}_\alpha = -\frac{\partial \psi}{\partial \alpha}$ is here identified the thermodynamic force associated in the (chemical) dissipation to the reaction rate $\dot{\alpha}$.

The thermodynamic restriction Eq. (8) can be split into three parts, i.e., the local actions $\mathcal{D}_1$, the chemical reaction $\mathcal{D}_2$, and the heat conduction $\mathcal{D}_3$, which are detailed as

$$\begin{aligned} &\mathcal{D}_1 = \left(\boldsymbol{\sigma} - \frac{\partial \psi}{\partial \boldsymbol{\varepsilon}^e}\right) \colon \dot{\boldsymbol{\varepsilon}}^e - \left(\frac{\partial \psi}{\partial T} + S\right)\dot{T} + \mathcal{A}_d \dot{d}, \\ &\mathcal{D}_2 = \mathcal{A}_\alpha \dot{\alpha}, \\ &\mathcal{D}_3 = -\boldsymbol{q} \cdot \frac{\nabla T}{T}. \end{aligned} \tag{9}$$

It has been shown that the positive of $\mathcal{D}$ will be obviously ensured if $\mathcal{D}_1$, $\mathcal{D}_2$ and $\mathcal{D}_3$ are all positive. Furthermore, we assume that the elastic strain rate $\dot{\boldsymbol{\varepsilon}}^e$, and temperature rate $\dot{T}$ can have arbitrarily prescribed values and they are independent of the rate of the order parameter. Hence, we can now apply the Coleman's exploitation to Eq. $(9)_1$, yielding two constitutive relations for the stress $\boldsymbol{\sigma}$, and the entropy S as

$$\boldsymbol{\sigma} = \partial_{\boldsymbol{\varepsilon}^e} \psi, \quad \text{and} \quad S = -\partial_T \psi. \tag{10}$$

2.3. Specification of dissipation and constitutive model

We here further specify the coupled problems, for instance, (i) chemo-thermal problem, (ii) mechanical problem, and (iii) phase field problem. The constitutive model and the strong-form equations in a thermodynamically consistent framework are thus derived.

2.3.1. Chemo-thermal problem

The thermodynamic force associated with the chemical dissipation $\mathcal{A}_\alpha$, which has been introduced in Eq. (9), can be rewritten as

$$\mathcal{A}_\alpha = -\frac{\partial \psi}{\partial \alpha} = -\Big[\frac{\partial \psi^e}{\partial \alpha} + \frac{\partial \psi^d}{\partial \alpha} + \frac{Q_\infty}{T_0}(T - T_0)\Big] - \frac{\partial h(\alpha)}{\partial \alpha}. \tag{11}$$

We assume that stress and fracture variations do not alter the thermodynamic imbalance between the chemical constituents of the hydration reaction. Hence, this eliminates the first term $\frac{\partial \psi^e}{\partial \alpha}$ and the second term $\frac{\partial \psi^d}{\partial \alpha}$ of $\mathcal{A}_\alpha$. Moreover the third term $\dfrac{Q_\infty}{T_0}(T - T_0)$ is considered to be negligible in regard of the usual range of temperature in the applications of concrete materials [8]. The chemical affinity can now be reformulated as

$$\mathcal{A}_\alpha = -\frac{\partial h(\alpha)}{\partial \alpha}. \tag{12}$$

Basically, the evolution of hydration degree is governed by the thermodynamic imbalance between unhydrated/hydrated cement [1], and this process is usually assumed to be thermoactivated. Therefore, an Arrhenius law can be employed to describe such problem

$$\dot{\alpha} = \hat{\mathcal{A}}_\alpha e^{\left(\dfrac{-E_a}{RT}\right)}, \tag{13}$$

where E_a is the activation energy; $R = 8.314 \times 10^{-3}$ [kJ K^{-1} mol^{-1}] is the ideal gas constant; and $\hat{\mathcal{A}}_\alpha = \frac{\mathcal{A}_\alpha}{\eta_\alpha}$, with η_α being the viscosity coefficient.

Note that, with this choice of the evolution equation for the hydration degree Eq. (13), the positive dissipation $\mathcal{D}_2$ is obviously ensured as

$$\mathcal{D}_2 = \mathcal{A}_\alpha \dot{\alpha} = \frac{\mathcal{A}_\alpha^2}{\eta_\alpha}\, e^{\left(\dfrac{-E_a}{RT}\right)} \geq 0. \tag{14}$$

In numerical model, $\hat{\mathcal{A}}_\alpha$ plays the role as an affinity, which characterizes the hydration kinetics. This function is often obtained through experimental data of an adiabatic calorimetric test. In this study, the formulation proposed in [39] is adopted as

$$\hat{\mathcal{A}}_\alpha = \frac{A_T}{Q_\infty} f(\alpha), \tag{15}$$

where the parameter A_T stands for the ratio of the maximum heat production rate to the latent hydration heat within a normalized definition of the hydration function; and $f(\alpha)$ is the chemical affinity function, representing the evolution of the normalized heat production rate in terms of the hydration degree.

In this analysis, $f(\alpha)$ is approximated by the power form [39]:

$$f(\alpha) = \left(\frac{\alpha}{a}\right)^b \left(\frac{1-\alpha}{1-a}\right)^c \tag{16}$$

in which the three constants a, b, and c are identified based on the experimental data.

The thermal equation can be constructed (in its entropy rate form) based on the first and second principles of thermodynamics. In the absence of the external volume heat source, the thermal equation can be expressed as

$$T_0 \dot{S} = -\nabla \cdot \boldsymbol{q} + \mathcal{D}. \tag{17}$$

The dissipation $\mathcal{D}$ is often eliminated. Using the constitutive relations for entropy S in (10), and assuming that the latent heat due to deformation released is negligible, it yields $T_0\dot{S} = \rho c\dot{T} - Q_\infty \dot{\alpha}$, along with (17). One can obtain

$$\rho c\dot{T} - Q_\infty \dot{\alpha} = -\nabla \cdot \boldsymbol{q}. \tag{18}$$

In Eq. (18), $Q_\infty \dot{\alpha}$ is the heat produced by the hydration reaction, and is defined as

$$Q_\infty \dot{\alpha} = A_T f(\alpha) e^{\left(\frac{-E_a}{RT}\right)}. \tag{19}$$

By adopting the Fourier's law $\boldsymbol{q} = -\boldsymbol{k}\nabla T$, the thermal problem can then be formulated as

$$\rho c\dot{T} = \nabla\left(\boldsymbol{k}\nabla T\right) + Q_\infty \dot{\alpha}, \tag{20}$$

in which $\boldsymbol{k}$ is the local thermal conductivity matrix influenced by fracture process, and is given by [22]

$$\boldsymbol{k} = g(d)\boldsymbol{k}_0, \tag{21}$$

where $\boldsymbol{k}_0$ is the thermal conductivity of the intact material, $g(d) = (1-d)^2 + \epsilon$ (with $\epsilon \ll 1$) is the degradation function, satisfying $g(0) \approx 1$, $g(1) \approx 0$ and $g'(1) = 0$, see Refs. [31, 34]).

Clearly, with the use of the Fourier's law, the positive restriction for $\mathcal{D}_3$

$$\mathcal{D}_3 = -\mathbf{q} \cdot \frac{\nabla T}{T} = \frac{\nabla T \; \boldsymbol{k} \; \nabla T}{T} \geq 0, \tag{22}$$

is satisfied.

According to Eqs. (19) and (20), the strong-form equations of the chemo-thermal problem are defined as a set of coupled equations to be solved on the domain $\Omega \in \mathbb{R}^D$ with its boundary $\partial\Omega$

$$\begin{cases} \rho c \dot{T} = \nabla\left(\boldsymbol{k}\nabla T\right) + Q_\infty \dot{\alpha} & \text{in } \Omega, \\ Q_\infty \dot{\alpha} = A_T f(\alpha)\,\exp(-E_a/RT) & \text{in } \Omega, \\ T = \overline{T} & \text{on } \partial\Omega_D, \\ \mathbf{n}^{\mathrm{T}}\big(-\boldsymbol{k}\nabla T\big) = \overline{q} + h\left(T_s - T_a\right) & \text{on } \partial\Omega_N. \end{cases} \tag{23}$$

The associated thermal boundary conditions are assumed to be a mixed boundary condition, described as follows:

$$T = \overline{T} \qquad \text{on} \qquad \partial\Omega_D, \tag{24}$$

and

$$\mathbf{n}^{\mathrm{T}}\big(-\boldsymbol{k}\nabla T\big) = \overline{q} + h\left(T_s - T_a\right) \qquad \text{on} \qquad \partial\Omega_N, \tag{25}$$

where $\overline{T}$ and $\overline{q}$ are respectively the prescribed temperature and heat flux at the Dirichlet Ω_D and Neumann Ω_N boundaries.

The convection condition is represented by the second term $h\left(T_s - T_a\right)$ in Eq. (25), with T_s and T_a representing the body surface and air temperature, respectively. As reported in Ref. [22], the convection coefficient h is found to be dependent upon a given wind speed at the solid surface and upon a given air temperature.

2.3.2. Age effects

The hardening process induced the development of mechanical property can be modeled by the age effects [11, 40]. The increase of the Young's modulus E, Poisson's ratio ν, and fracture resistance g_c is expressed as functions of the hydration degree, which is explicitly described as follows:

$$\begin{cases} E(\alpha) = E_\infty \overline{\alpha}^{\alpha_E}, \\ \nu(\alpha) = 0.18\,\sin\dfrac{\pi\alpha}{2} + 0.5\,e^{-10\alpha}, \\ g_c(\alpha) = g_{c\infty}\overline{\alpha}^{\alpha_{g_c}}, \end{cases} \tag{26}$$

where E_∞ is the final Young's modulus, $g_{c\infty}$ is the final fracture energy, and the functions $\overline{\alpha}^{\alpha_E}$, $\overline{\alpha}^{\alpha_{g_c}}$ are however chosen as reported in Refs. [11, 40]

$$\overline{\alpha}^{\alpha_E} = \left\langle \frac{\alpha - \alpha_E}{1 - \alpha_E} \right\rangle_+ \qquad \text{and} \qquad \overline{\alpha}^{\alpha_{g_c}} = \left\langle \frac{\alpha - \alpha_{g_c}}{1 - \alpha_{g_c}} \right\rangle_+, \tag{27}$$

in which $< . >_+$ denotes the positive operator; α_E and α_{g_c} are two material constants, which define moment when the material begins to have the strength.

2.3.3. Mechanical problem

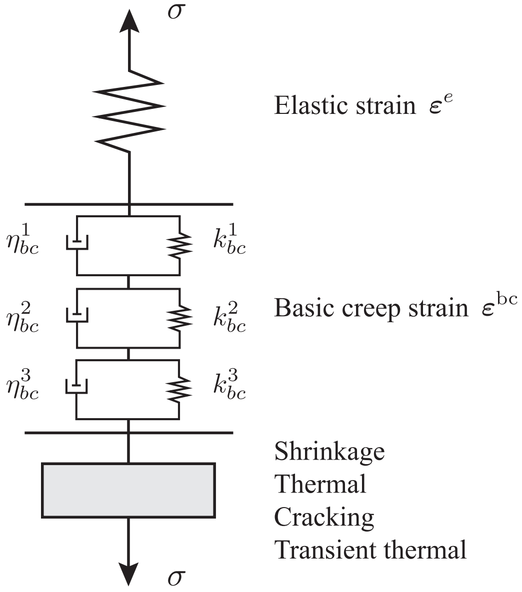

Figure 2: Description of the proposed model for complex mechanical response during hydration process.

The mechanical problem can be schematically sketched in Fig. 2, where the effects of chemo-thermal process and creep at early-age are all included in the present model. It implies that the following expression of the elastic strain reaches:

$$\boldsymbol{\varepsilon}^e = \frac{1}{2}\Big((\nabla \mathbf{u})^{\mathrm{T}} + (\nabla \mathbf{u}) \Big) - \boldsymbol{\varepsilon}^{\mathrm{th}} - \boldsymbol{\varepsilon}^{\mathrm{au}} - \varepsilon^{\mathrm{ttc}} - \varepsilon^{\mathrm{bc}}, \tag{28}$$

where $\boldsymbol{\varepsilon}^{\mathrm{th}}$ is the thermal expansion strain, $\boldsymbol{\varepsilon}^{\mathrm{au}}$ is the autogenous shrinkage strain, $\boldsymbol{\varepsilon}^{\mathrm{ttc}}$ is the transient thermal creep strain, and $\boldsymbol{\varepsilon}^{\mathrm{bc}}$ is the basic creep strain.

Based on Ref. [22], the thermal strain and the autogenous shrinkage strain are defined as

$$\boldsymbol{\varepsilon}^{\mathrm{th}} = \beta(T - T_0)\mathbf{1} \quad \text{and} \quad \boldsymbol{\varepsilon}^{\mathrm{au}} = -\kappa \left\langle \frac{\alpha - \alpha_{au}}{1 - \alpha_{au}} \right\rangle_+ \mathbf{1}, \tag{29}$$

where β is the thermal expansion coefficient, κ is a material constant, and α_{au} represents a mechanical percolation threshold of the autogenous shrinkage. According to Ref. [41], the expression of the transient thermal creep is obtained as

$$\dot{\boldsymbol{\varepsilon}}^{\mathrm{ttc}} = \lambda_{\mathrm{ttc}} |\dot{T}| \boldsymbol{\sigma}, \tag{30}$$

in which λ_{ttc} is a material parameter characterizing the stress induced thermal strain due to the transient temperature history. An appropriate choice of such material parameter has previously been addressed in Refs. [4, 41], for instance, $\lambda_{\mathrm{ttc}} = 1.38 \times 10^{-12}$ Pa^{-1}K^{-1}.

The basic creep is modeled by rheological elements (spring and dashpots) using Kelvin-Voigt chain with three units combined in serial, see Fig. 2. The evolution of basic creep strain of the Kelvin-Voigt unit i is described through the following relationship [13, 15]

$$\tau_{bc}^{i}\ddot{\boldsymbol{\varepsilon}}_{bc}^{i} + \left(\tau_{bc}^{i}\frac{\dot{k}_{bc}^{i}(\alpha, T)}{k_{bc}^{i}(\alpha, T)}\right)\dot{\boldsymbol{\varepsilon}}_{bc}^{i} = \frac{\dot{\boldsymbol{\sigma}}}{k_{bc}^{i}(\alpha, T)}. \tag{31}$$

The spring stiffness k_{bc}^{i} and dash-pot viscosity η_{bc}^{i} are affected by the temperature and by the hydration degree as

$$k_{bc}^{i}(\alpha, T) = k_{bc\infty}^{i}\frac{0.473\alpha^{0.62}}{2.081 - 1.608\alpha}e^{\left(\frac{E_{ac}}{R}\left(\frac{1}{T} - \frac{1}{T_0^{bc}}\right)\right)}, \tag{32}$$

and

$$\eta_{bc}^{i}(\alpha, T) = \eta_{bc}^{i}(\alpha, T_0^{bc})e^{\left(\frac{E_{ac}}{R}\left(\frac{1}{T} - \frac{1}{T_0^{bc}},\right)\right)}. \tag{33}$$

In Eqs. (32) and (33), E_{ac} is the creep activation energy, which can be identified from experimental data, and $T_0^{bc} = 293$ K is taken for this analysis. The characteristic time τ_{bc}^{i} in Eq. (31) is kept to be independent from the temperature

$$\tau_{bc}^{i} = \frac{\eta_{bc}^{i}(\alpha)}{k_{bc}^{i}(\alpha)}. \tag{34}$$

Once the elastic strain $\boldsymbol{\varepsilon}^{e}$ has been well defined. We now provide the explicit form of the density of strain energy. In order to maintain the compressive resistance during crack closure, the unilateral contact model is used. The formulation, which is proposed by Miehe et al. [34] with the assumption that damage induced by traction only, is noticed being suitable for brittle material such as concrete. Herein, the density of elastic energy for the isotropic materials can be written as

$$\psi^{e} = g(d)\ \psi^{e+}\left(\boldsymbol{\varepsilon}^{e}\right) + \psi^{e-}\left(\boldsymbol{\varepsilon}^{e}\right). \tag{35}$$

The positive and negative parts of the strain energy $\psi^{e\pm}(\boldsymbol{\varepsilon}^{e})$ in Eq. (35) are defined by

$$\psi^{e\pm}(\boldsymbol{\varepsilon}^{e}) = \frac{\lambda}{2}\big[\left\langle \operatorname{tr}\boldsymbol{\varepsilon}^{e}\right\rangle_{\pm}\big]^{2} + \mu \operatorname{tr}\big[\left(\boldsymbol{\varepsilon}^{e\pm}\right)^{2}\big], \tag{36}$$

where ε^{e+} and ε^{e-} are, respectively, the extensive and compressive modes of the elastic strain tensor $\boldsymbol{\varepsilon}^{e} = \boldsymbol{\varepsilon}^{e+} + \boldsymbol{\varepsilon}^{e-}$, and its derivatives with respect to the elastic strain defines two projection tensor

$$\mathbb{P}^{\pm}(\boldsymbol{\varepsilon}^{e}) = \partial_{\boldsymbol{\varepsilon}^{e}}\left[\boldsymbol{\varepsilon}^{e\pm}(\boldsymbol{\varepsilon}^{e})\right]. \tag{37}$$

Basically, $\mathbb{P}^{\pm}(\boldsymbol{\varepsilon}^e)$ can be determined as described in [42], and curious readers may refer to, e.g., Ref. [43], for detail of numerical implementation.

The Euler-Lagrange equations of the variational principle for mechanical problem can be expressed as

$$\mathbf{u}(\mathbf{x}) = Arg\left\{ \inf_{\mathbf{u}\in\mathcal{S}_u} \left(E(\boldsymbol{\varepsilon}^e, d, \alpha, T) - W^{ext} \right) \right\}, \tag{38}$$

where $\mathcal{S}_u = \left\{ \mathbf{u} | \mathbf{u}(\mathbf{x}) = \bar{\mathbf{u}} \text{ on } \partial\Omega_D, \quad \mathbf{u} \in H^1(\Omega) \right\}$ and $W^{ext} = \int_\Omega \mathbf{f}\cdot\mathbf{u}\,\mathrm{d}\Omega + \int_{\partial\Omega_N} \overline{\mathbf{F}}\cdot\mathbf{u}\,\mathrm{d}\Gamma$ with $\mathbf{f}$ being the body force, while $\overline{\mathbf{F}}$ representing the prescribed traction over the boundary $\partial\Omega_N$. The strong form of the mechanical problem can then be expressed as follows:

$$\begin{cases} \nabla\cdot\boldsymbol{\sigma} + \mathbf{f} = \mathbf{0} & \text{in } \Omega, \\ \mathbf{u} = \bar{\mathbf{u}} & \text{on } \partial\Omega_D, \\ \boldsymbol{\sigma}\mathbf{n} = \overline{\mathbf{F}} & \text{on } \partial\Omega_N, \end{cases} \tag{39}$$

in which, $\bar{\mathbf{u}}$ is the prescribed displacement on the boundary $\partial\Omega_D$.

2.3.4. Phase field problem

Here we will present a crack phase field evolution law that ensures the irreversibility of the process. From Eqs. (9), (10), (14), and (22), a reduced form of the Clausius-Duhem inequality can be expressed as

$$\mathcal{A}_d\dot{d} \geq 0. \tag{40}$$

At this stage, we introduce a threshold function $F(\mathcal{A}_d)$ such that

$$F(\mathcal{A}_d) \leq 0. \tag{41}$$

The principle of maximum dissipation requires the dissipation $\mathcal{A}_d\dot{d}$ to be maximum under the constraint defined in Eq. (41). To archive this aim, the method of Lagrange multipliers is employed:

$$\mathcal{L} = -\mathcal{A}_d\dot{d} + \lambda F(\mathcal{A}_d). \tag{42}$$

The corresponding Kuhn-Tucker equations are

$$\frac{\partial\mathcal{L}}{\partial\mathcal{A}_d} = 0, \quad \lambda \geq 0, \quad F \leq 0, \quad \lambda F = 0. \tag{43}$$

Without loss of generality, the threshold function $F(\mathcal{A}_d)$ is assumed in the form $F(\mathcal{A}_d) = \mathcal{A}_d$. Using the first and the second inequalities in the Kuhn-Tucker equations (43), one reaches

$$\dot{d} = \lambda \frac{\partial F(\mathcal{A}_d)}{\partial \mathcal{A}_d} = \lambda \geq 0. \tag{44}$$

In case of crack growth, $\dot{d} > 0$, regarding Eq. (44), it provides $\lambda > 0$. From the last equality in Eq. (43), we obtain $F = 0$, or $\mathcal{A}_d = 0$. Hence, the following law for the crack propagation is obtained

$$F = \mathcal{A}_d = -\frac{\delta \psi}{\delta d} = -\frac{\partial \psi^e}{\partial d} - g_c \delta\gamma(d, \nabla d) = 0, \tag{45}$$

where $\delta\gamma(d, \nabla d)$ defines the variational derivative of the crack density function [34]

$$\delta\gamma(d, \nabla d) = \frac{d}{l} - l\Delta d. \tag{46}$$

From Eqs. (35), and (45), the evolution law for the phase field d is obtained as

$$2(1-d)\psi^{e+} - g_c \delta\gamma(d, \nabla d) = 0. \tag{47}$$

The criteria of irreversible evolution of cracks can be verified as follows. As $2(1-d)\psi^{e+} \geq 0$, Eq. (47) ensures $\delta\gamma(d, \nabla d) \geq 0$, and due to Eq. (44), we can check the variation of crack length

$$\dot{\Gamma}_l = \int_\Omega \delta\gamma(d, \nabla d)\dot{d} \ \mathrm{d}\Omega \geq 0. \tag{48}$$

As a consequence, the proposed model is to be consistent with the thermodynamic axiom of positive dissipation, satisfying the irreversibility constraint of crack evolution.

The local crack driving force $\mathcal{H}(\mathbf{x}, t)$ is also introduced to ensure the positive of Eq. (48). It describes a dependence on history [34], and to make loading-unloading possible

$$\mathcal{H}(\mathbf{x}, t) = \underset{\tau \in [0,t]}{max} \left\{ \frac{\ell}{g_c(\alpha)} \psi^{e+}(\mathbf{x}, \tau) \right\}. \tag{49}$$

Basically, $\mathcal{H}(\mathbf{x}, t)$ contains the maximum reference energy, or a measure for the maximum tensile strain obtained in the deformation history, which provides a very transparent representation of the balance equation that governs the diffusive crack topology. For detailed information, curious readers should refer to, e.g., Refs. [34, 43].

From Eqs. (46), (47), and (49), the final expression of the evolution law for the phase field reaches

$$2(1-d)\mathcal{H} - \left(d - \ell^2 \Delta d\right) = 0 \ \text{ in } \Omega, \tag{50}$$

belong with a homogeneous Neumann condition $\nabla d(\mathbf{x}) \cdot \mathbf{n} = 0$ on $\partial\Omega$.

2.4. Numerical formulation

The coupled problems described in Eqs. (23), (50), and (39) are solved by utilizing a standard FE method integrated with a staggered procedure, i.e., we alternatively solve the chemo-thermal problem, phase field problem, and the mechanical problem. The detailed numerical implementation for each problem is provided in Appendix B.

3. Numerical examples and discussions

In this section, we first discuss the influence of some aspect parameters on the simulation results. In particular, the following three issues, which affect the numerical simulation results of fracture behavior, are examined: (i) the loading increments size, (ii) the mesh size, and (iii) the capacity of the unilateral contact condition. Then, we will conduct numerical simulations in both mesoscopic and macroscopic scales to show the performance of the present approach. Herein we consider one example at the structural scale, and the other one is devoted to the investigation of the influence of microstructural heterogeneity on fracture behavior of the structure. In all examples, the plane strain condition is adapted along with assumption that no thermal flux perpendicular to the plane is considered, which is to be consistent with the thick concrete structure.

One should be noticed that this work is dedicated to the development of new numerical schemes, comparison between the numerical prediction and experiment is thus not provided. However, the validation of the proposed model is confirmed though the demonstration of the computed results and the experimental investigation reported in our recent study [44].

3.1. Model analysis

A quarter of a circular solid containing a square hole made of concrete as schematically sketched in Fig. 3 is considered. The material parameters given in Ref. [15], and now listed in Table 1 are used. The critical hydration degree, in which cement material begins having its strength is taken as follows: $\alpha_E = 0.15$ for the Young's modulus and the same $\alpha_{g_c} = 0.15$ for fracture resistance. The autogenous shrinkage strain is activated once the hydration degree gets greater than $\alpha_{au} = 0.115$, as described in Eq. (29). The Poisson's ratio is assumed to be independent of the hydration process and $\nu = 0.2$ is taken. Three Kelvin-Voigt units are used to model basic creep, where the spring stiffness and dash-pot viscosity are chosen, and detailed in Table 1 [13, 15].

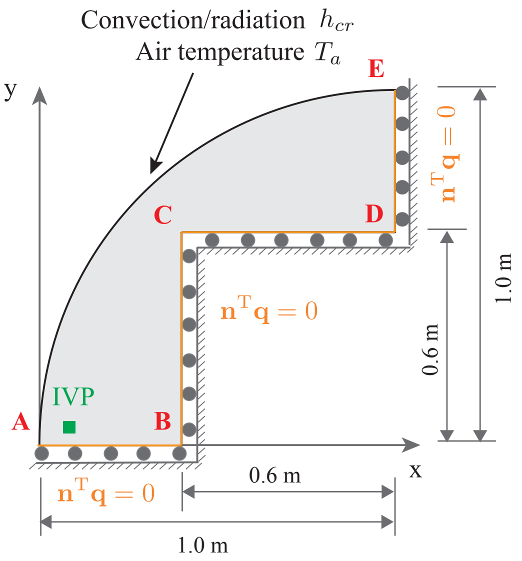

Figure 3: Geometry and boundary conditions of benchmark example, a quarter of a circular solid containing a square hole made of concrete subjected to the mixed boundary conditions.

Table 1: Material properties (Ref. [15])

Pmt	Value	Unit	Pmt	Value	Unit
ρc	2400	kJ/(K.m^3)	α_{au}	0.115	-
k	2.8	W/(m.K)	α_E	0.15	-
Q_∞	117840	kJ/m^3	α_{g_c}	0.15	-
h_{cr}	4	W/(m^2.K)	E_{ac}	17.4	kJ/mol
β	4	µm/(m.K)	ν	0.2	-
κ	80	µm/m	T_a	20	°C
E_∞	35	GPa	A_T	0.215	GW/kg
g_c	32.5	N/m	E_a	44.929	kJ/mol
$k^1_{bc,\infty}$	1000	GPa	$\tau^1_{bc,\infty}$	0.1	Days
$k^2_{bc,\infty}$	650	GPa	$\tau^2_{bc,\infty}$	1	Days
$k^3_{bc,\infty}$	100	GPa	$\tau^3_{bc,\infty}$	10	Days

In phase field model, as discussed in Appendix A, the internal length ℓ is computed through the relationship with the material parameters (E, g_c) and the tensile strength σ_c, as

$$\ell = \frac{27 E g_c}{256 \sigma_c^2}. \tag{51}$$

With the tensile strength of concrete as $\sigma_c = 3.45$ MPa, the internal length ℓ finally reaches an approximate value of 10 mm. This value is sufficiently small as compared to the structure size.

Different types of thermal and mechanical boundary conditions are assigned to the considered structure as detailed in Fig. 3 and Table 2. The investigated system is in convection with air environment on the arc AE, which is modeled by the convection/radiation coefficient $h_{cr} = 4$ W/(m^2.K) and $T_a = 20°$C. For the mechanical boundary conditions: the $y-$ displacements are fixed at two edges AB and CD, while the $x-$ displacements are here free; and the $x-$ displacements are fixed at two edges BC and DE, while the $y-$ displacements are set to be free. Both $x-$ and $y-$ displacements are kept freely on the arc AE. The plane strain condition is assumed to all numerical analyses.

3.1.1. Influence of time increments

The effects of the time increments on the chemo-thermo-mechanical and fracture behavior are numerically analyzed. The investigated structure is discretized with meshes using triangular elements. In particular, a fine mesh of 71727 triangular elements with $h_e = 2.5$ mm is used, that satisfies the condition $\ell \geq 2h_e$ for having several elements inside the diffused region. Several time increments taken from $\Delta t = 300$ s to $\Delta t = 1500$ s have been considered. The evolution of the temperature and hydration degree is then plotted in Figs. 4, and 5 for the investigated point IVP ($x = 0.2$ m, $y = 0.1$ m). The obtained results indicate that the influences of the time increment on the thermal and hydration processes are insignificant and they can be negligible.

Table 2: Description of boundary conditions

Edge	Thermic	Ux	Uy
AB, CD	Zero flux	Free	Block
BC, DE	Zero flux	Block	Free
AE	Convection h_{cr}, T_a	Free	Free

To investigate the effects of the time increment on the numerical solution of the creep and mechanical response, the overall creep strains and overall stress at the edge DE (average value) are calculated. The obtained results for the $xx-$ component are then represented in Fig. 6, and 7, showing a good convergence. The variations of creep strain and stress are below 3 % when the increment goes from 500 s to 300 s. This confirms the stability of the easy-to-implement staggered algorithm as soon as sufficiently small loading steps are used. Too large steps tend to delay the initiation/propagation of damage and thus harden the overall response of the structure, see Fig. 8.

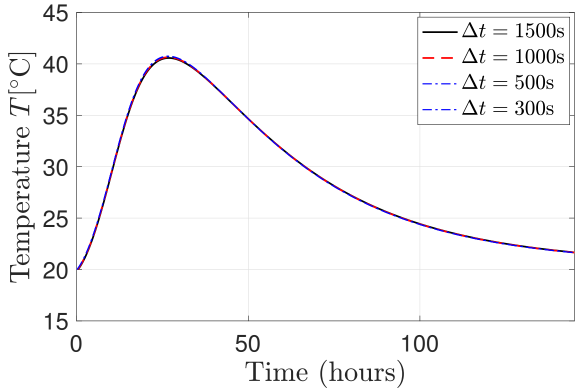

Figure 4: Temperature evolution at an investigated position in the solid domain for different time increments. The influences of the time increments on the thermal problem are very small.

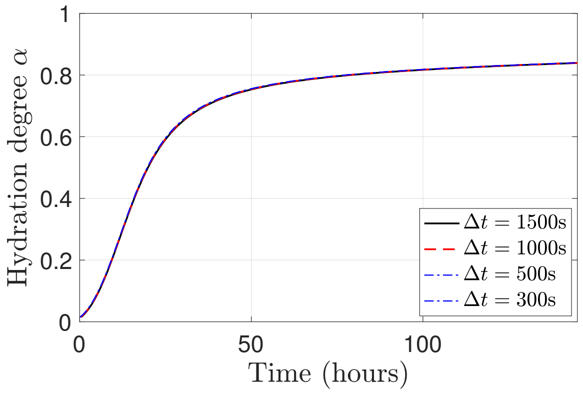

Figure 5: Hydration evolution at an investigated position in the solid domain for different time increments. The influences of the time increment on the hydration process are negligible.

3.1.2. Influence of mesh size

The mesh size effect on the solutions is now considered. In particular, we investigate the convergence of the chemo-thermo-mechanical response with respect to mesh refinement. Here, an incremental time step as $\Delta t = 300$ s is selected. Then, several simulations using refined meshes are performed where the characteristic size of the elements varies between $h_e = 1$ mm and $h_e = 5$ mm.

The computed results are represented in Fig. 9 for the evolution of temperature and in Fig. 10 for the mechanical response. Based on the obtained numerical results, and similarly to the time increment effects, the mesh refinement does not significantly alter the thermal problem. The convergence of mechanical response is obtained. The mesh independent solution can be archived when the mesh size is taken to be sufficient small compared to the length scale ℓ, as discussed in [34, 38].

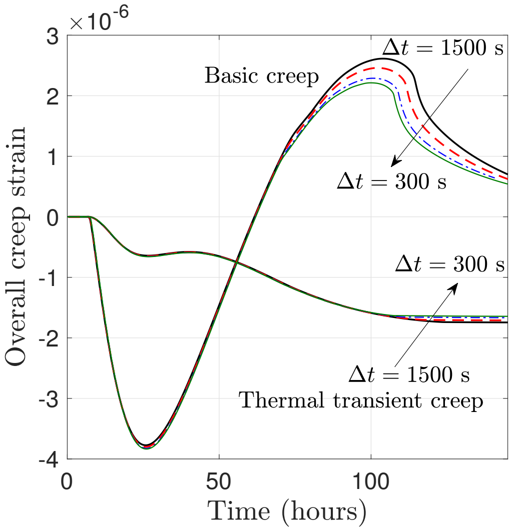

Figure 6: The evolution of basic creep strain $\varepsilon_{xx}^{\mathrm{bc}}$, and transient thermal creep strain $\varepsilon_{xx}^{\mathrm{ttc}}$ for different time increments. A good convergence of creep behavior with respect to the time increment is observed.

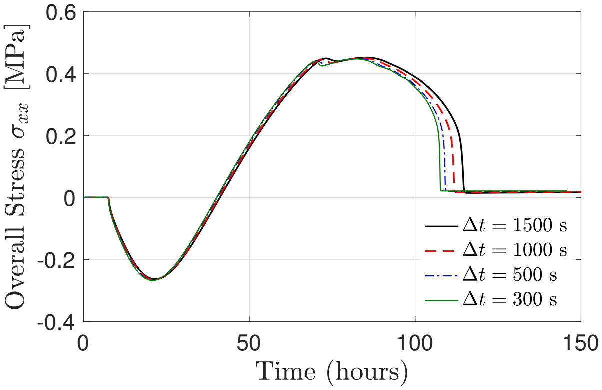

Figure 7: Convergence of the stress response with respect to the time increment.

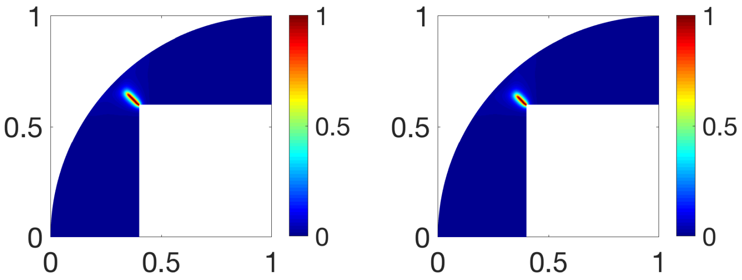

(a) $\Delta t = 300$ s

(b) $\Delta t = 1500$ s

Figure 8: Crack path at time $t = 100$ hours for different time increments.

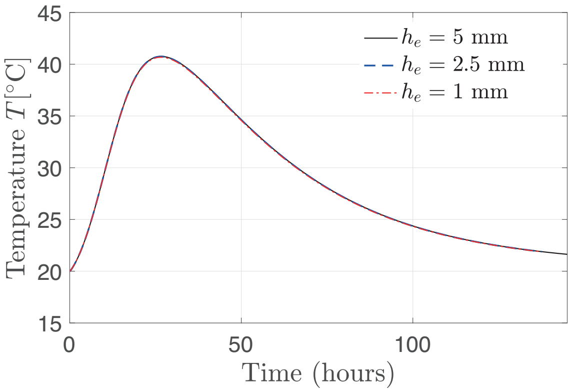

Figure 9: The evolution of temperature at an investigated position in the solid domain for different mesh size. The influences of the mesh refinement on the thermal problem are very small.

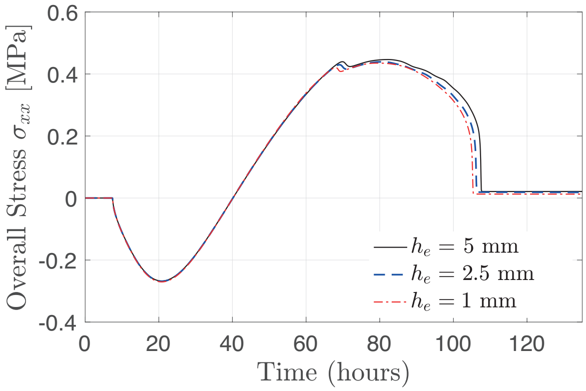

Figure 10: Convergence of the stress response with respect to the mesh refinement: the overall stress is evaluated at the edge DE (average value).

3.1.3. Unilateral contact capacities

In the last part of the model analysis, we investigate the capability of the unilateral contact formulation in handling auto-contact in a cyclic loading problem (loading/unloading situation). For this purpose, the same domain as described in Fig. 3 is reconsidered. The traction conditions are prescribed on the edges AB and DE of the structure at the age 50 hours after casting, see Fig. 11(a) for a detailed description of the boundary conditions.

The evolution of the prescribed displacements is depicted in Fig. 11(b), in which loading and unloading procedures are applied. The overall loading curve is provided in Fig. 12. Herein the average of stress in the $x-$ direction is plotted with respect to the prescribed displacement. It is noted that within the time period $t = [2 - 4s]$, the structure is unloaded until compression mode. Clearly,

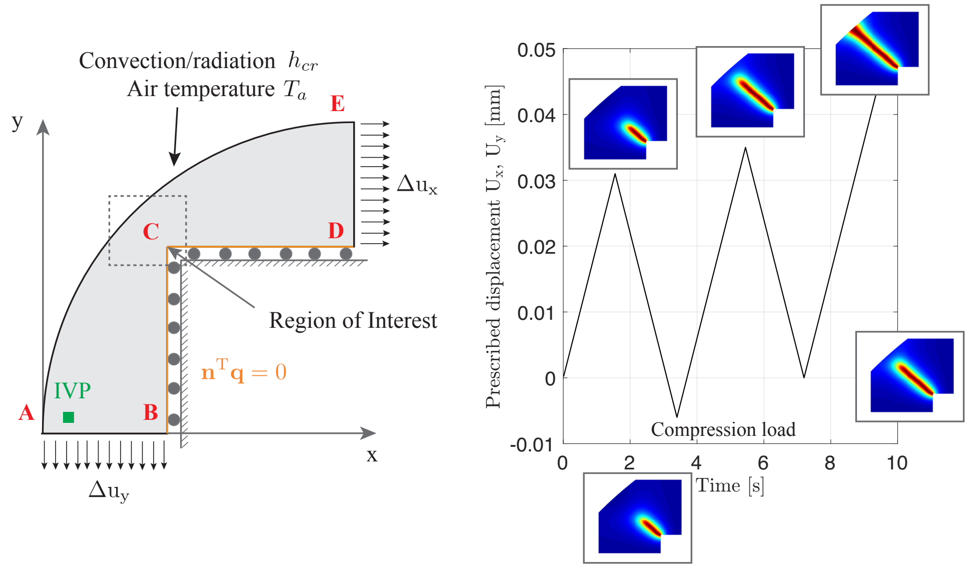

(a) Geometry and boundary conditions. (b) Evolution of the prescribed displacement.

Figure 11: Description of the studied problem to verifying the unilateral contact capacities.

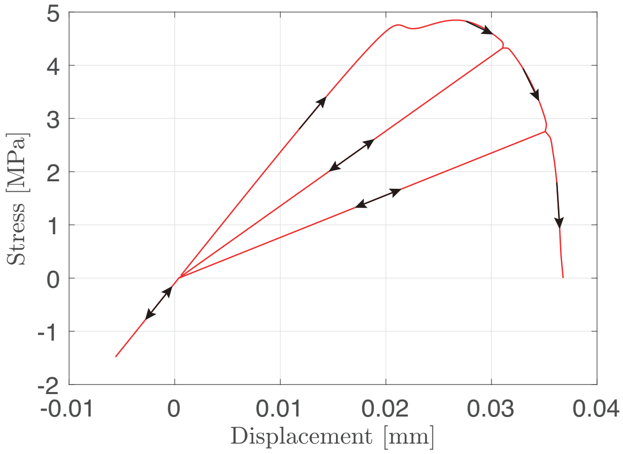

Figure 12: Stress - displacement curve obtained from the loading and unloading problem.

the auto-contact at the crack lips is demonstrated. The asymmetric behavior in traction and in compression of concrete materials is also captured in Fig. 12.

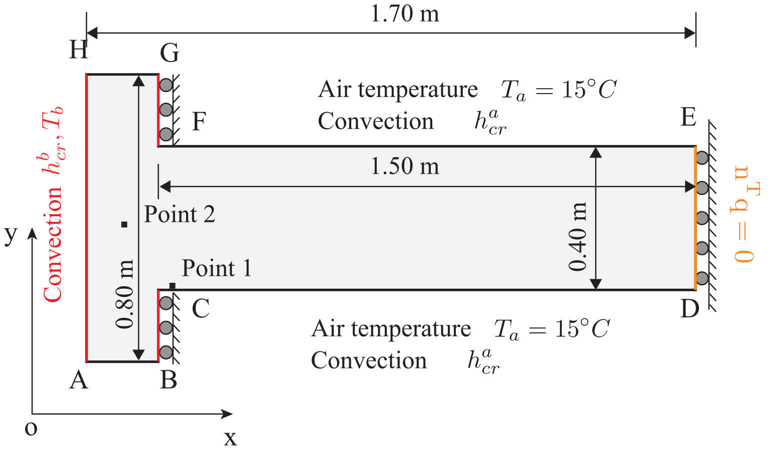

Figure 13: Geometry and boundary conditions of the investigated system, a T-Shape structure is subjected to different convection conditions.

A T-shape solid structure made of concrete as shown in Fig. 13 is considered. The same material parameters given in Table 1 of the previous example are used. The structure is subjected to different types of thermal and mechanical boundaries conditions as depicted in Fig. 13 and detailed in Table 3. The investigated system is in convection with air environment at four edges: AB, CD, EF and GH. This interaction is modeled by the convection/radiation coefficient $h^a_{cr} = 6$ W/(m^2.K) and air temperature $T_a = 15$°C. The lower convection/radiation coefficient $h^b_{cr} = 3 \times 10^{-4}$ W/(m^2.K) is used for three edges AH, BC, FG to describe the convection of the system with other regions, e.g., when the sample is in contact with wrapped materials with $T_b = 20$°C. The Dirichlet boundary conditions are also applied to block the displacement in the $x-$direction at three edges BC, DE, FG. Such a setup will provide a critical working condition of the structure, in which damage could take place.

Table 3: Description of boundary conditions

Edge	Thermic	Ux	Uy
AB, CD, EF, GH	Convection h^a_{cr}, T_a	Free	Free
BC, FG	Convection h^b_{cr}, T_b	Block	Free
DE	Zero flux	Block	Free
AH	Convection h^b_{cr}, T_b	Free	Free

The structure is discretized using triangular elements. As usual, a set of fine meshes of 388428 triangular elements (e.g., $h_e^{min} = 1.5$ mm) is applied to the critical zones to which cracks could initiate, whereas a coarse mesh (e.g., $h_e^{max} = 10$ mm) is for the rest of the body.

Basically, this designed mesh should meet the condition $\ell > 2h_e$ for having several elements inside the diffused region. The incremental time step is taken as $\Delta t = 300$ s for the total of 2500 time steps. The initial conditions $T_0 = 20°\text{C}$ and $\alpha_0 = 0.01$ are chosen for the whole system. The plane strain condition is assumed for this analysis.

The evolution of the hydration degree at two investigated positions located at $(x_1 = 225, y_1 = 210)$ mm and $(x_2 = 100, y_2 = 400)$ mm is computed and their results are then shown in Fig. 15. It has been shown that the hydration evolves quickly at the beginning period of the hardening process, generating the heat that is more than the heat loss due to convection to the environment, and resulted in the increase of temperature as exhibited in Fig. 14. The temperature reaches its maximum value at time $t \approx 22.5$ hours and then decreases corresponding to the decelerated period of hydration process. The development of material strength (i.e., the Young's modulus and fracture resistance) is also illustrated in Fig. 15, and a similar phenomenon is observed. The concrete material quickly gains 70% of its strength after 48 hours.

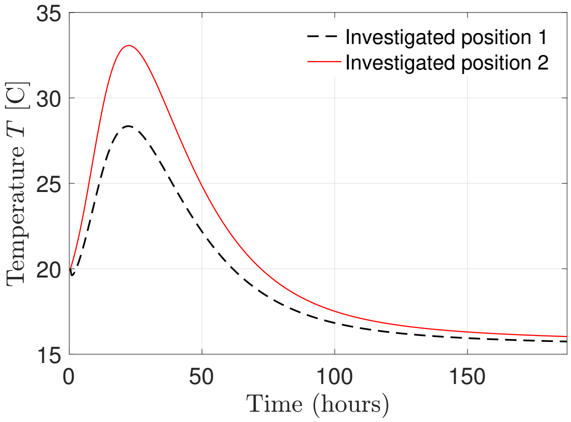

Figure 14: Temperature evolution at different positions in the solid domain: the structure reaches the maximum temperature at time $t = 22.5$ hours and then decreases in time.

Next, the local distribution of temperature, hydration degree, and damage level (phase field variable) of the considered structure at several time steps is estimated and their results are then shown in Fig. 16. Due to shrinkage, two cracks symmetrically initiate at two corners at time $t \approx 62.50$ hours. With the cooling of the system and the increase of autogenous shrinkage, we clearly observe the growth of these two cracks. The structure is completely collapsed at time $t = 142.5$ hours. To demonstrate the crucial role of creeping at early-age, we then provide in Fig. 17 a comparison of

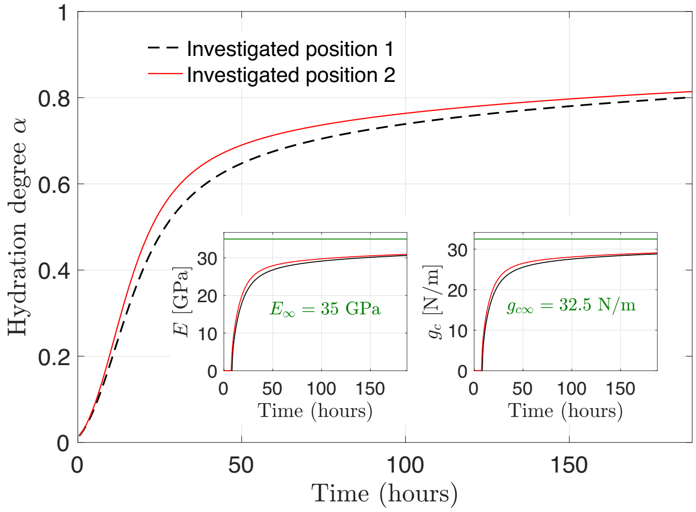

Figure 15: Evolution of the hydration and material strength (i.e., the Young's modulus and fracture resistance) at different positions in the investigated solid domain.

fracture response between two cases, i.e., with and without consideration of creep. We capture that the model without consideration of creep predicts crack initiation earlier. The structure is also collapsed sooner, at $t = 100$ hours in comparison with $t = 142.5$ hours for the case of including creep effects. It implies that the presence of creep reduces tensile stress and hence delays the occurrence/propagation of cracks. In other words, the relaxation of stress due to creep improves the cracking and post-cracking resistance of the concrete structure.

The evolution of elastic strain in $x-$ direction for both cases with and without consideration of the creep effects, (computed at edge DE) is plotted in Fig. 18. In the model with consideration of the creep effects, we also plot the basic creep strain and transient thermal creep strain. The same delayed phenomenon as in the stress evolution is observed. These results have confirmed the important role of creep effects when studying the early-age behavior of cement-based materials. It strongly alters the cracking response of the structure.

3.3. Early-age cracking in a heterogeneous concrete structure at the mesoscopic scale

We now consider the microstructural effects on the early-age behavior of the concrete materials. A sub-structure with dimension $L \times H = 2 \times 2$ cm^2 is investigated, in which the microstructural details are explicitly taken into account, see Fig. 19. An image-based model obtained from microtomography of a concrete consisting of coarse sand embedded into a cement matrix is used. The considered 2D microstructure is a cross-section of CT-images obtained by the XRCT laboratory scanner available at

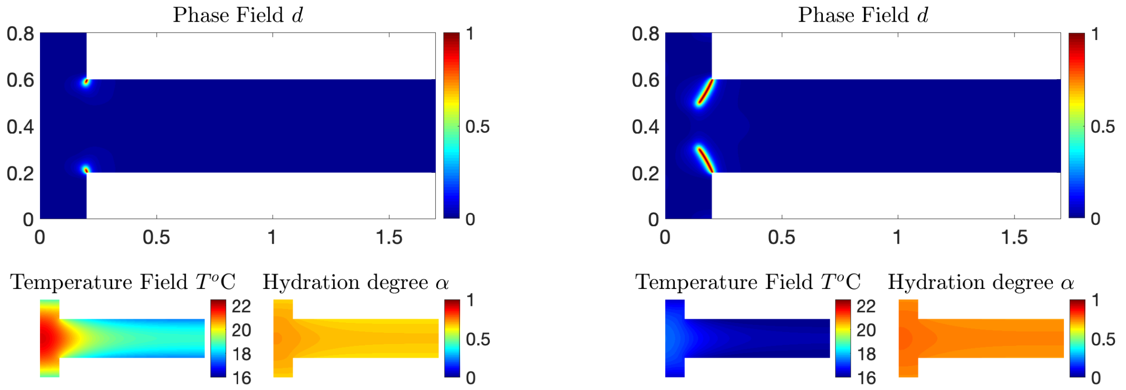

(a) time $t = 62.50$ hours b) time $t = 104.17$ hours

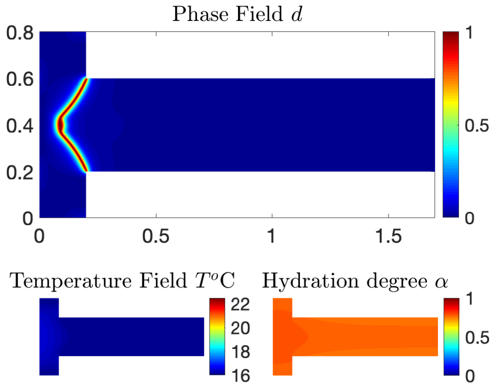

(c) time $t = 142.50$ hours

Figure 16: The evolution of the phase field, temperature, and hydration degree of the structure during the hydration process calculated by the present approach. The shrinkage strain resulted in crack nucleation and growth at the two vertices.

Navier laboratory [45]. The grey level image was filtered and thresholded to separate two phases of the microstructure. The computed result is represented in Fig. 19, where the white and black phases correspond to the matrix (cement paste), inclusions (sand grains), respectively.

In this example, our main goal is to capture the risk of early-age cracking in cement-based material when it is subjected to a thermal treatment. This is a crucial procedure in manufacture of the special fiber reinforced concrete using shape memory alloys (requiring a heat treatment). The material and model parameters for two phases: sand grains and cement matrix at the mesoscopic scale are listed in Table 4 [46–48]. Moreover, a strong assumption is made for the proposed model at this scale: *the*

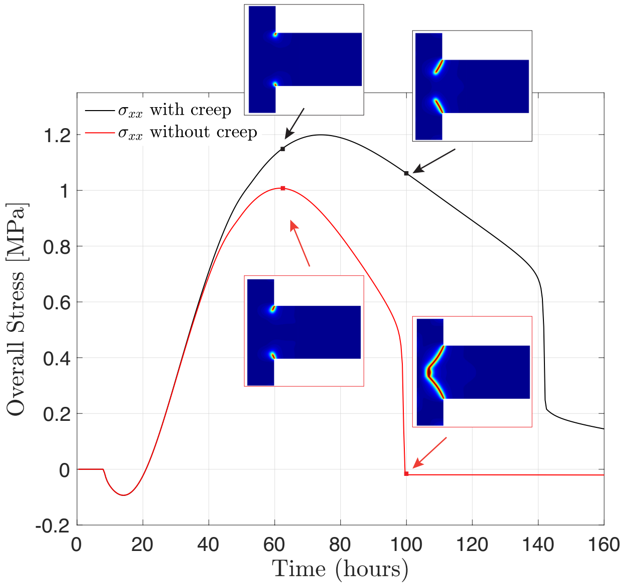

Figure 17: The evolution of overall stress σ_{xx} at edge DE during hardening process; comparison between two cases with and without considering the creep effects.

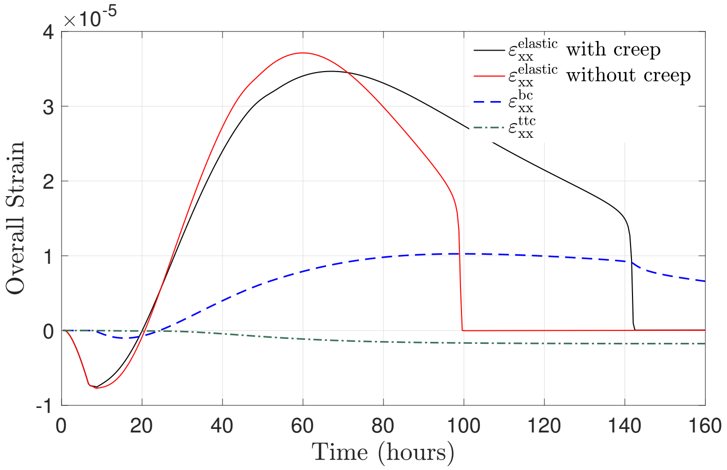

Figure 18: The evolution of basic creep strain $\varepsilon_{xx}^{\rm bc}$, transient thermal creep strain $\varepsilon_{xx}^{\rm ttc}$, and elastic strain $\varepsilon_{xx}^{\rm elastic}$ for two cases, with and without consideration of the creep effects.

hydration process will only take place in the cement matrix, and so only this phase is affected by creep effects. This assumption was made by considering that the creep is due to the viscous behavior of C-S-H restrained by the elastic phases in the cement paste, see e.g., [49, 50] for more detail.

The mixed boundary conditions are used to mimic the thermal condition of the heat treatment acting on the sub-structure. More specifically, the convection condition and Dirichlet boundary condition $T = \overline{T}$ are alternatively applied on the upper-end EF ($y = 10$ cm), while the left-end AF is

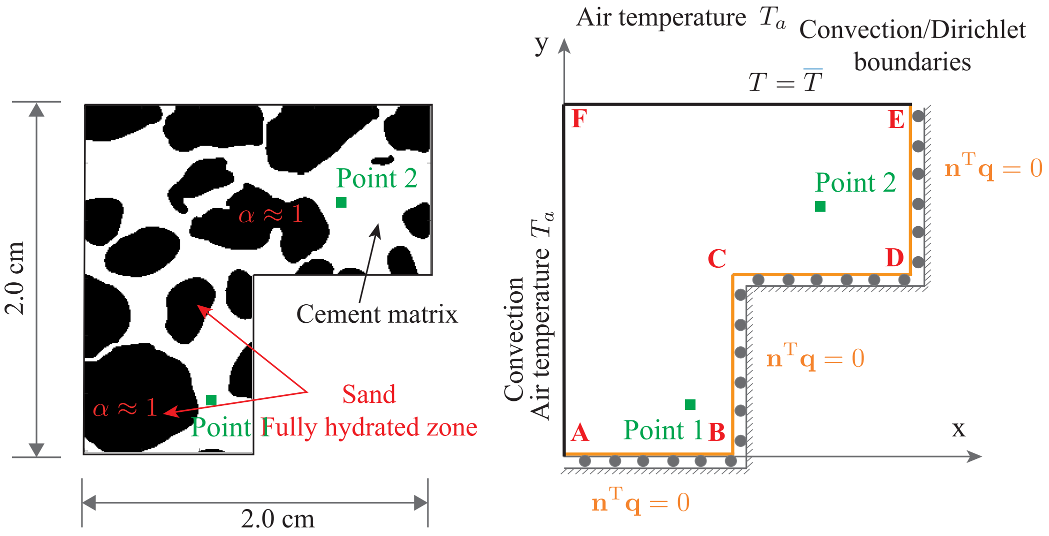

Figure 19: Geometry and boundary conditions of a solid structure, where the microstructural heterogeneities are explicitly taken into account.

Table 4: Material properties

Parameter	Cement matrix	Sand	Unit
ρc	2415	2337	kJ/(K.m^3)
k	1.55	3.2	W/(m.K)
Q_∞	908443	-	kJ/m^3
β	12	5	μm/(m.K)
κ	200	10^{-10}	μm/m
E_∞	18	50	GPa
g_c	18	120	N/m
σ_c	2	8	MPa
α_{au}	0.115	-	-
α_E	0.15	-	-
α_{g_c}	0.15	-	-
ν	0.22	0.3	-
T_0	20	20	°C
A_T	0.215	-	GW/kg
E_a	38.3	-	kJ/mol

only affected by the convection condition. The displacements in both $x, y-$ directions of these two edges AF and EF are kept to be free. The four edges AB, BC, CD, DE with orange color are subjected to zero flux condition, with the displacement's constraint that is defined as follows: on the edges AB and CD, displacements in $y-$ direction are fixed while displacements in $x-$ direction are free; on the edges BC and DE, displacements in $x-$ direction are fixed while displacements in $y-$ direction are free. The details of mixed boundary conditions are described in Table 5.

Table 5: Description of boundary conditions

	Thermal boundary conditions		Mechanical boundary conditions	
	$t = [0 - 69.31]$ hours	$t > 69.31$ hours	$x-$displacements	$y-$displacements
AB	Zero flux	Zero flux	Free	Block
BC	Zero flux	Zero flux	Block	Free
CD	Zero flux	Zero flux	Free	Block
DE	Zero flux	Zero flux	Block	Free
EF	Convection $T_a = 20°\text{C}$	Dirichlet $\overline{T} = 105°$	Free	Free
AF	Convection $T_a = 20°\text{C}$	Convection $T_a = 20°\text{C}$	Free	Free

From the 500 × 500 pixels, a mesh of ≈ 375000 triangular elements (e.g., a mesh size with $h_e = 0.04$ mm), is generated. The material property of matrix and inclusion are transferred into the triangular domains associated with elements. A detailed description was previously reported by the present authors, and curious readers should refer to, see e.g., [43] for more information. The simulation begins with a time step, e.g., $\Delta t = 200$ s, and at the moment of switching to the Dirichlet boundary conditions of the heat transfer problem ($t > 69.31$ hours), it is reduced to $\Delta t = 3$ s.

The results of crack propagation, temperature evolution, and development of hydration are then shown in Fig. 20. It should be noticed here that a post-processing procedure is adopted to highlight the effects of sand on the fracture problem. The geometry of sand grains is represented and marked in blue color, which is then overlaid with the phase field. Furthermore, the global strain and stress are computed by taking the average value at the edge AB (lower-end $y = 0$), and plotted in Figs. 21, 22 for the $xx-$ component. In general, we observe two periods of the mechanical fracture behavior corresponding to the two different thermal boundary conditions, as follows:

(i) Time period $t = [0 - 69.31]$ hours: Classical hydration process, where the shrinkage crack is observed.

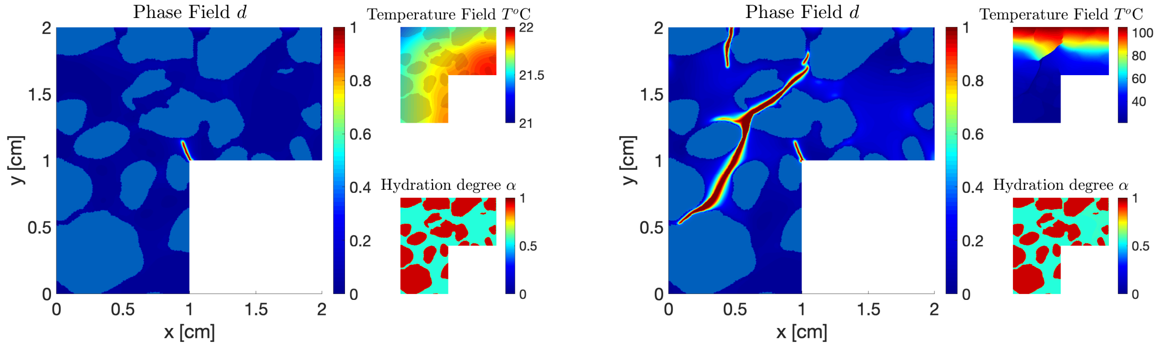

(a) time $t = 69.31$ hours (b) time $t = 69.50$ hours

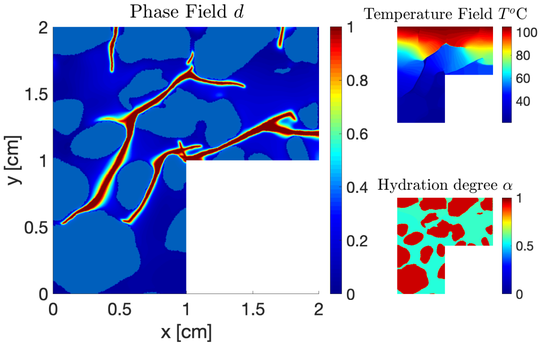

(c) time $t = 69.65$ hours

Figure 20: Evolution of damage level, temperature, and hydration for several time steps. The phase field is plotted in the left figure for each time step. The obtained results have demonstrated a strong effect of microstructural heterogeneity on the crack propagation tendency.

(ii) Time period $t > 69.31$ hours: Thermal shock period, in which a sudden change of strain and stress is captured along with the presence of complex crack networks.

More specifically, at the first period, the cracking due to the shrinkage/hydration is observed at the structure's corner at time $t \approx 40$ hours after casting. Then it propagates until reaching the sand grain as depicted in Fig. 20(a) for the time $t = 69.31$ hours. The presence of damage provides a non-linear development of strain and stress at this period, see Figs. 21 and 22. The strain evolution has demonstrated again the important role of the basic creep strain on the global behavior of the structure. Effects of the transient thermal creep can be negligible, which is due to the small variation of temperature during the hydration period (less than 7°C). At the second period, the thermal treatment introduces a sudden change in the thermo-mechanical fracture behavior of the structure. The temperature quickly rises and induces the initiation/propagation of several new crack networks.

A strong effect of heterogeneity on the fracture phenomena is captured. The cracks mostly propagate in the interfacial region of cement/sand. More interestingly, we observe the initiation of interfacial crack, that then links to the main crack as shown in Fig. 20(b),(c).

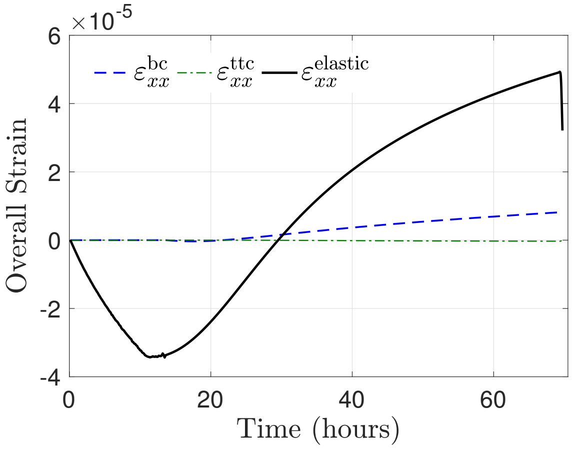

Figure 21: Evolution of transient thermal creep train, basic creep strain, and elastic strain during the hardening process of the investigated system.

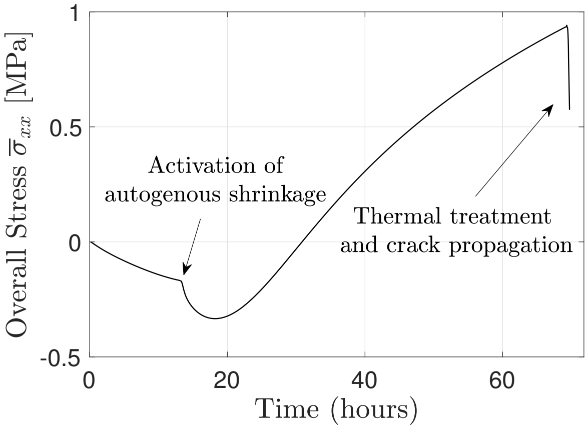

Figure 22: Comparison of numerical results of stress development between the homogeneous structure and the heterogeneous structure. A significant difference due to the effects of heterogeneities is captured.

The evolution of the temperature at two investigated positions (denoted Point 1 and Point 2 in Fig. 19) is plotted in Fig. 23, where we also provide two other zoom-in plots of the time and temperature scales of interest. The obtained results are quasi identical for both positions at the first time period $t = [0 - 69.31]$ hours. However, at the second time period $t > 69.31$ hours, the temperature in the region close to the upper-end is much higher than in other regions. Note that, cracks are assumed to be insulating in this work, *i.e*, that does not allow thermal transfer crossing cracked region. Hence, we observe a strong variation of thermal distribution between the lower and upper parts of the investigated structure. This phenomenon is recognized as the major reason for the cracking problem captured in Fig. 20, where cracks are mostly distributed in the upper zone, and mainly propagate following the horizontal direction (this tendency is also affected by the distribution of sand grains).

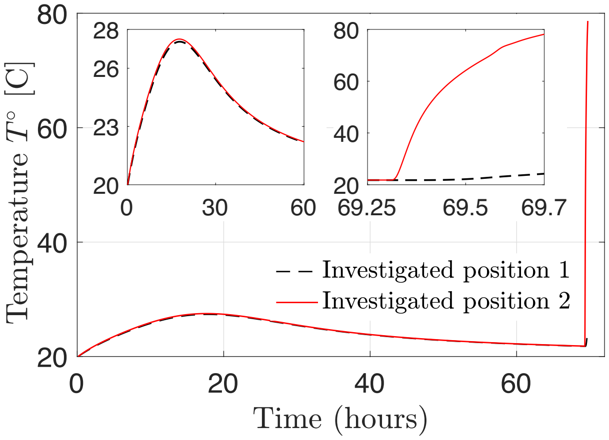

Figure 23: Evolution of temperature at two investigated points during the hydration process.

The observation of this numerical experiment has demonstrated a high risk of early-age cracking for cement-based materials, particularly when they are subjected to thermal treatment. The very complex chemo-thermo-mechanical/fracture behavior at the mesoscopic scale is obtained as the strong effects of heterogeneity on the fracture phenomena are captured. The influence of basic creep strain is also significant. All of that confirms the important role of creep and microstructural details, which are highly required to model the early-age behavior of the cement-based materials accurately. The obtained results also demonstrate the performance of the proposed model, which is applicable to the large-scale study of the hydration induced crack propagation from the micrometer scale to the meter scale. It is particularly suitable for investigation of strongly heterogeneous material at the microscopic level and its effect on macroscopic behavior. The new model is promising to develop a concurrent multi-scale model with a complete description of the multi-physics processes at the microscopic scale.

3.4. Summary of the computational time

In all cases, a workstation with 18 cores, 112 Go Ram and 2.4 GHz processor was used (see https://hpc.uni.lu/systems/iris/). The present code has been implemented in Matlab.

Table 6: Computational time for the different examples.

Problem	No. Elements	No. Increments	CPU-time/increment	Total CPU-time
Model analysis	71727	1800	5.30 [s]	2.65 [hours]
T-Shape solid structure	388428	2250	48.31 [s]	30.19 [hours]
Heterogeneous concrete	375000	1750	56.72[s]	27.57 [hours]

4. Conclusion

In this paper, we have developed a new multi-physics computational framework based on the phase field model for studying the early-age cracking behavior of cement-based materials. The influences of hydration, material strength's development, thermal transfer, shrinkage, and both basic/transient thermal creeps on fracture behavior are fully considered. A new constitutive law has been developed to include the creep effects, where the mechanical problem is solved directly from the stress equilibrium equation at an investigated time (instead of incremental stress). The new scheme is suitable to make use of unilateral contact formulation at crack surfaces. It provides a strong coupling with fracture mechanics in the variational approach of the phase field model. Compared with the models proposed in the literature, the new model describes better the interactions of damage with multi-physics processes of hydration. The accuracy of the method has been proved through a benchmark analysis of the mesh size, time increment effects, and the capacity of the unilateral contact condition. Specially, thanks to the advantage of the phase field model with the advanced local crack driving force, our developed model is able to capture all fracture stages such as crack nucleation, initiation and propagation in the complex heterogeneous material under arbitrary loading conditions.

The present model is extremely robust. With the use of the staggered update scheme, the solution of the multi-physics problem can be obtained by solving: (i) one non-linear problem for updating the temperature and hydration degree; (ii) two linear problems for updating the phase field, and the displacement field. Moreover, this scheme increases the computational efficiency of the method, which is promising to investigate a complex problem in 3D.

We have successfully applied the proposed model to study the thermal-mechanical behavior of the structure at the macroscopic scale, in which the heat of hydration, the evolution of material strength, and the crack propagation are all simulated in an efficient way. We also performed the analysis of fracture phenomena at the mesoscopic scale, where the microstructural heterogeneities are explicitly taken into account. The effects of creep at different length scales are also analyzed and discussed. The obtained results indicate that the creep and details of microstructure play an important role in evaluating the mechanical behavior of concrete after casting.

5. Acknowledgments

The support this work from SeRaMCo project (Secondary Raw Materials for Concrete Precast Products), through the transnational cooperation projects in North-West Europe (Interreg NWE), NWE-320, is gratefully acknowledged.

Appendix A. Choice of the regularization parameter ℓ

The choice of ℓ has previously been discussed in Refs. [37, 38]. In the aforementioned works, the regularized length in the phase field model is considered as an internal parameter (related to the material properties) that affects the critical stress at which crack nucleation occurs. Therefore, the internal length has to be identified from material parameters. A relationship between ℓ and material parameters has been established by considering uniaxial traction of a bar, as follows:

$$\sigma_c = \frac{3}{16}\sqrt{\frac{3}{2}}\sqrt{\frac{E g_c}{\ell}}, \tag{A.1}$$

where σ_c is the critical value of stress in traction.

Some recent phase field models have been presented to eliminate the sensibility of the length scale on the mechanical response [51, 52]. However, these models seem to be computationally expensive.

Appendix B. Numerical implementations

Appendix B.1. Chemo-thermal problem

A standard Newton–Raphson method is employed to solve the nonlinear problem defined by Eq. (23). It yields the following linear system, which is solved at each iteration

$$\begin{cases} \dfrac{\partial \boldsymbol{\mathcal{R}}_T}{\partial \mathbf{T}^e}\tilde{\mathbf{T}} = -\boldsymbol{\mathcal{R}}_T, \\ \\ \dfrac{\partial \boldsymbol{\mathcal{R}}_\alpha}{\partial \boldsymbol{\alpha}^e}\tilde{\boldsymbol{\alpha}} = -\boldsymbol{\mathcal{R}}_\alpha. \end{cases} \tag{B.1}$$

The time integration is modeled by using the Euler method, *i.e.*, $\dot{x}_{n+1} = (x_{n+1} - x_n)/\Delta t$. The tangential matrix at time step $n+1$ reads

$$\frac{\partial \boldsymbol{\mathcal{R}}_T}{\partial \mathbf{T}^e_{n+1}} = \mathbf{K}_T + \frac{1}{\Delta t}\mathbf{H}_T + \mathbf{Q}_c - \frac{\partial \mathbf{F}_\alpha}{\partial \mathbf{T}^e_{n+1}}, \tag{B.2}$$

and

$$\frac{\partial \boldsymbol{\mathcal{R}}_\alpha}{\partial \boldsymbol{\alpha}^e_{n+1}} = \frac{1}{\Delta t}\mathbf{Q}_\alpha - \frac{\partial \mathbf{F}_\alpha}{\partial \boldsymbol{\alpha}^e_{n+1}}, \tag{B.3}$$

in which

$$\frac{\partial \mathbf{F}_\alpha}{\partial \mathbf{T}^e_{n+1}} = \int_\Omega \mathbf{N}_T^{\mathrm{T}} \bigg(A_T f(\alpha) \frac{E_a}{RT^2}\ e^{-E_a/RT} \bigg) \mathbf{N}_T \ \mathrm{d}\Omega,$$

and

$$\frac{\partial \mathbf{F}_\alpha}{\partial \boldsymbol{\alpha}^e_{n+1}} = \int_\Omega \mathbf{N}_\alpha^{\mathrm{T}} \bigg(A_T \frac{\partial f(\alpha)}{\alpha}\ e^{-E_a/RT} \bigg) \mathbf{N}_\alpha \ \mathrm{d}\Omega.$$

For the definition of each component matrix, the reader is referred to [22] for more practical information.

Appendix B.2. Mechanical problem

Assuming that the spring stiffness and dash-pot viscosity are constants within each time step, the incremental basic creep strain is computed as follows

$$\Delta \boldsymbol{\varepsilon}^{bc}_{n+1} = \boldsymbol{\varepsilon}^{bc}_{n+1} - \boldsymbol{\varepsilon}^{bc}_{n} = \mathbf{A}^{bc}_1 + \mathbf{A}^{bc}_2 \cdot \boldsymbol{\sigma}_n + \mathbf{A}^{bc}_3 \cdot \boldsymbol{\sigma}_{n+1}, \tag{B.4}$$

where $\mathbf{A}^{bc}_1, \mathbf{A}^{bc}_2, \mathbf{A}^{bc}_3$ are three second-order tensors (for more detail, curious readers should refer to, e.g., see [13]). These three tensors depend on material parameters, incremental time step and stress in the dashpot $\boldsymbol{\sigma}^{i,\mathrm{ds}}$, which will be updated at the end of each time step.

For the Kelvin-Voigt unit i, the stress in the dashpot reads

$$\boldsymbol{\sigma}^{i,\mathrm{ds}}_{n+1} = \Delta \boldsymbol{\sigma}_{n+1} \frac{\overline{\tau}^i_{bc}}{\Delta t} \left(1 - e^{1-\Delta t/\overline{\tau}^i_{bc}} \right) + \boldsymbol{\sigma}^{i,\mathrm{ds}}_{n} e^{1-\Delta t/\overline{\tau}^i_{bc}}. \tag{B.5}$$

The incremental transient thermal creep strain can be written as follows

$$\Delta \boldsymbol{\varepsilon}^{\mathrm{ttc}}_{n+1} = \boldsymbol{\varepsilon}^{\mathrm{ttc}}_{n+1} - \boldsymbol{\varepsilon}^{\mathrm{ttc}}_{n} = \mathbf{T}^{ttc} \cdot \left(\boldsymbol{\sigma}_n + \boldsymbol{\sigma}_{n+1} \right), \tag{B.6}$$

with $\mathbf{T}^{ttc}$ being the second-order tensor, depending on $t_{ttc} = \lambda_{ttc} \left(\frac{T_{n+1} - T_n}{2} \right)$ and the Poisson's ratio.

The Cauchy stress tensor at time step $n+1$ is defined according to the constitutive relation (10) by

$$\boldsymbol{\sigma}_{n+1} = \mathbf{C}_d \bigg(\nabla^s \mathbf{u}_{n+1} - \boldsymbol{\varepsilon}^{\mathrm{th}}_{n+1} - \boldsymbol{\varepsilon}^{\mathrm{au}}_{n+1} - \boldsymbol{\varepsilon}^{\mathrm{bc}}_{n+1} - \boldsymbol{\varepsilon}^{\mathrm{ttc}}_{n+1} \bigg), \tag{B.7}$$

where $\mathbf{C}_d$ is the matrix form of fourth-order tensor $\mathbb{C}(d)$ in Voigt notation.

By introducing the indicator $\mathcal{R}^{\pm}$, with

$$\mathcal{R}^+_n = \mathrm{sign}\left(\mathrm{tr}\, \boldsymbol{\varepsilon}^e_n \right), \quad \text{and} \quad \mathcal{R}^-_n = 1 - \mathcal{R}^+_n \left(\varepsilon^e \right), \tag{B.8}$$

where sign(.) = 1 if (.) ≥ 0, and, sign(.) = 0 if (.) < 0.

It implies the general expression for elastic stiffness accounting for damage as

$$\mathbf{C}_d = g(d)\left[\lambda(\alpha)\mathcal{R}_n^+[\mathbf{1}]^{\mathrm{T}}[\mathbf{1}] + 2\mu(\alpha)\mathbf{P}_n^+\right] + \left[\lambda(\alpha)\mathcal{R}_n^-[\mathbf{1}]^{\mathrm{T}}[\mathbf{1}] + 2\mu(\alpha)\mathbf{P}_n^-\right]. \tag{B.9}$$

where $\mathbf{P}_n^{\pm}$ is the matrix form of $\mathbb{P}_n^{\pm}$ (see Eq. (36)) in Voigt notation [43]

From Eqs. (B.4), (B.6), (B.7), the new formulation for Cauchy stress in the incremental scheme is thus rewritten

$$\boldsymbol{\sigma}_{n+1} = \mathbf{C}_d^c\left[\nabla^s\mathbf{u}_{n+1} - \boldsymbol{\varepsilon}_{n+1}^{\mathrm{th}} - \boldsymbol{\varepsilon}_{n+1}^{\mathrm{au}} - \left[\boldsymbol{\varepsilon}_n^{\mathrm{bc}} + \boldsymbol{\varepsilon}_n^{\mathrm{ttc}} + \mathbf{A}_1^{bc} + \left(\mathbf{A}_2^{bc} + \mathbf{T}^{ttc}\right)\boldsymbol{\sigma}_n\right]\right], \tag{B.10}$$

with

$$\mathbf{C}_d^c = \mathbf{C}_d\left[\mathbf{1} + \mathbf{C}_d\mathbf{A}_3^{bc} + \mathbf{C}_d\mathbf{T}^{ttc}\right]^{-1}. \tag{B.11}$$

Above, $\mathbf{C}_d^c$ can be considered as the effective stiffness, accounting for damage and corrected by creep effects.

Remark: In the works proposed by [13, 15], the transient thermal creep strain and basic creep strain are assumed to be induced by effective stress (without consideration of damage). It means that the interaction among fracture, mechanical problem and creeps are neglected. In order to get a stronger coupled model of fracture mechanics and multi-physics process of cement hydration, the creep strains are here assumed to be induced by apparent stress, involving the stress degradation cause of damage. Consequently, the proposed scheme dominates over the existing approaches [13, 15]. More specifically, the present model is able to capture the decrease of creep strain rate due to the stress relaxation (during crack propagation). In addition, the mechanical problem will be directly considered by using final Cauchy stress instead of incremental stress. This is needed for the use of unilateral contact formulation on the fracture assessment.

The displacement problem to be solved at time t_{n+1} is expressed by seeking $\mathbf{u}(\mathbf{x}) \in S_u$, such that

$$\int_\Omega \nabla^s\mathbf{u}_{n+1}\ \mathbf{C}_d^c\ \nabla^s\delta\mathbf{u}\ \mathrm{d}\Omega = \int_\Omega \mathbf{C}_d^c\Big[\boldsymbol{\varepsilon}_{n+1}^{\mathrm{th}} + \boldsymbol{\varepsilon}_{n+1}^{\mathrm{au}} + \\ + \left[\boldsymbol{\varepsilon}_n^{\mathrm{bc}} + \boldsymbol{\varepsilon}_n^{\mathrm{ttc}} + \mathbf{A}_1^{bc} + \left(\mathbf{A}_2^{bc} + \mathbf{T}^{ttc}\right)\boldsymbol{\sigma}_n\right]\Big]\nabla^s\delta\mathbf{u}\ \mathrm{d}\Omega. \tag{B.12}$$

The linear system of equations is obtained for time step $n+1$ as follows

$$\mathbf{K}_u\mathbf{u}_{n+1} = \mathbf{F}_u, \tag{B.13}$$

where

$$\mathbf{K}_u = \int_\Omega \mathbf{B}_u^{\mathrm{T}} \, \mathbf{C}_d^c \, \mathbf{B}_u \, \mathrm{d}\Omega, \tag{B.14}$$

and

$$\mathbf{F}_u = \int_\Omega \mathbf{B}_u^{\mathrm{T}} \mathbf{C}_d^c \Big(\boldsymbol{\varepsilon}_{n+1}^{\mathrm{th}} + \boldsymbol{\varepsilon}_{n+1}^{\mathrm{au}} + \boldsymbol{\varepsilon}_n^{\mathrm{bc}} + \boldsymbol{\varepsilon}_n^{\mathrm{ttc}} + \mathbf{A}_1^{bc} + \Big(\mathbf{A}_2^{bc} + \mathbf{T}^{ttc} \Big) \boldsymbol{\sigma}_n \Big) \, \mathrm{d}\Omega. \tag{B.15}$$

Appendix B.3. Phase field problem

Using the variational principle for Eq. (50), it yields the following phase field problem to be solved at time t_{n+1}

$$\int_\Omega \Big(2\mathcal{H}_{n+1} + 1 + \frac{\eta_d}{\Delta t} \Big) d_{n+1} \delta d \, \mathrm{d}\Omega + \int_\Omega \ell^2 \nabla d_{n+1} \nabla \delta d \, \mathrm{d}\Omega = \int_\Omega \Big(2\mathcal{H}_{n+1} + \frac{\eta_d}{\Delta t} d_n \Big) \delta d \, \mathrm{d}\Omega. \tag{B.16}$$

The linear system of equations is given by

$$\mathbf{K}_d \mathbf{d}_{n+1} = \mathbf{F}_d, \tag{B.17}$$

where

$$\mathbf{K}_d = \int_\Omega \mathbf{N}_d^{\mathrm{T}} \Big(2\mathcal{H}_{n+1} + 1 + \frac{\eta_d}{\Delta t} \Big) \mathbf{N}_d \, \mathrm{d}\Omega + \int_\Omega \ell^2 \mathbf{B}_d^{\mathrm{T}} \mathbf{B}_d \, \mathrm{d}\Omega, \tag{B.18}$$

$$\mathbf{F}_d = \int_\Omega \mathbf{N}_d^{\mathrm{T}} \Big(2\mathcal{H}_{n+1} + \frac{\eta_d}{\Delta t} d_n \Big) \, \mathrm{d}\Omega. \tag{B.19}$$

Appendix B.4. Key steps of solution algorithm

The main steps of the solution procedure (or pseudo codes) are briefly described

- **Initialization**

  (a) Initialize the temperature field $T_0(\mathbf{x})$, the hydration degree field $\alpha_0(\mathbf{x})$, and its time derivatives $\dot{T}_0(\mathbf{x})$, $\dot{\alpha}_0(\mathbf{x})$.

  (b) Initialize the displacement field $\mathbf{u}_0(\mathbf{x})$, the phase field $d_0(\mathbf{x})$, and the history functional $\mathcal{H}_0 = 0$.

  (c) Initialize the basic creep strain $\boldsymbol{\varepsilon}_0^{\mathrm{bc}}(\mathbf{x}) = 0$, the transient thermal creep strain $\boldsymbol{\varepsilon}_0^{\mathrm{ttc}}(\mathbf{x}) = 0$, the dashpot stress $\boldsymbol{\sigma}_0^{i,\mathrm{ds}}(\mathbf{x}) = 0$, and Cauchy stress $\boldsymbol{\sigma}_0(\mathbf{x}) = 0$.

- **FOR** $t^{n+1} \leq t^{\max}$, given T_n, $\dot{T}_n$, α_n, $\dot{\alpha}_n$ $\mathbf{u}_n$, d_n, $\mathcal{H}_n$, $\boldsymbol{\varepsilon}_n^{\mathrm{bc}}$, $\boldsymbol{\varepsilon}_n^{\mathrm{ttc}}$, $\boldsymbol{\sigma}_n^{i,\mathrm{ds}}$, and $\boldsymbol{\sigma}_n$.

  (1) Chemo-thermal problem

. Compute $\mathbf{T}_{n+1}$ and $\boldsymbol{\alpha}_{n+1}$ by solving the iterative scheme Eq. (B.1).

(2) Account age effects

. Material parameters are updated by taking into account the age effects Eqs. (26), (32), (33).

(3) Displacement problem

. (i) Compute $\mathbf{P}_n^{\pm}$, $\mathcal{R}_n$ according to [34, 43].

. (ii) Compute $\mathbf{A}_{1,2,3}^{bc}$, $\mathbf{T}^{ttc}$ by Eq. (B.6), and $\boldsymbol{\varepsilon}_{n+1}^{\mathrm{th}}$ and $\boldsymbol{\varepsilon}_{n+1}^{\mathrm{au}}$ by Eq. (29).

. (iii) Compute $\mathbf{K}_u$ and $\mathbf{F}_u$ and then displacement field $\mathbf{u}_{n+1}(\mathbf{x})$ by solving problem (B.13).

(4) Supplementary

. (i) Compute Cauchy stress $\boldsymbol{\sigma}_{n+1}$ by Eq. (B.10), and dashpot stress $\boldsymbol{\sigma}_{n+1}^{i,\mathrm{ds}}$ according to Eq. (B.5).

. (ii) Compute $\boldsymbol{\varepsilon}_{n+1}^{\mathrm{bc}}$ and $\boldsymbol{\varepsilon}_{n+1}^{\mathrm{ttc}}$ by Eqs. (B.4), (B.6), and then elastic strain $\boldsymbol{\varepsilon}_{n+1}^{e}$ by Eq. (28).

(5) Phase field problem

. (i) Compute history field $\mathcal{H}_{n+1}(\mathbf{x}, \tau)$ by Eq. (49).

. (ii) Compute $\mathbf{K}_d, \mathbf{F}_d$ and then phase field $d_{n+1}(\mathbf{x})$ by solving problem Eq. (B.17).

$(.)_n \leftarrow (.)_{n+1}$ **and go to step (1).**

- **END**

References

[1] F-J. Ulm and O. Coussy. Modeling of thermochemomechanical couplings of concrete at early ages. *Journal of Engineering Mechanics*, 121(7):785–794, 1995.

[2] D.P. Bentz. A review of early-age properties of cement-based materials. *Cement and Concrete Research*, 38(2):196–204, 2008.

[3] Z.P. Bazant. *Mathematical modeling of creep and shrinkage of concrete.* Wiley, 1988.

[4] A.B. Hauggaard, L. Damkilde, and P.F. Hansen. Transitional thermal creep of early age concrete. *Journal of Engineering Mechanics*, 125(4):458–465, 1999.

[5] B. Bissonnette, M. Pigeon, and A.M. Vaysburd. Tensile creep of concrete: study of its sensitivity to basic parameters. *ACI Materials journal*, 104(4):360, 2007.

[6] M. Briffaut, F. Benboudjema, J-M. Torrenti, and G. Nahas. Concrete early age basic creep: Experiments and test of rheological modelling approaches. *Construction and Building Materials*, 36:373–380, 2012.

[7] R. de Borst and A.H. Van den Boogaard. Finite-element modeling of deformation and cracking in early-age concrete. *Journal of Engineering Mechanics*, 120(12):2519–2534, 1994.

[8] M. Cervera, J. Oliver, and T. Prato. Thermo-chemo-mechanical model for concrete. I: Hydration and aging. *Journal of Engineering Mechanics*, 125(9):1018–1027, 1999.

[9] M. Cervera, J. Oliver, and T. Prato. Thermo-chemo-mechanical model for concrete. II: Damage and creep. *Journal of Engineering Mechanics*, 125(9):1028–1039, 1999.

[10] Y. Yuan and Z.L. Wan. Prediction of cracking within early-age concrete due to thermal, drying and creep behavior. *Cement and Concrete Research*, 32(7):1053–1059, 2002.

[11] G. De Schutter. Finite element simulation of thermal cracking in massive hardening concrete elements using degree of hydration based material laws. *Computers & Structures*, 80(27-30): 2035–2042, 2002.

[12] Z.P. Bažant, J-K. Kim, and S-E. Jeon. Cohesive fracturing and stresses caused by hydration heat in massive concrete wall. *Journal of Engineering Mechanics*, 129(1):21–30, 2003.

[13] F. Benboudjema and J-M. Torrenti. Early-age behaviour of concrete nuclear containments. *Nuclear Engineering and Design*, 238(10):2495–2506, 2008.

[14] Y. Lee and J-K. Kim. Numerical analysis of the early age behavior of concrete structures with a hydration based microplane model. *Computers & Structures*, 87(17-18):1085–1101, 2009.

[15] M. Briffaut, F. Benboudjema, J.M. Torrenti, and G. Nahas. Numerical analysis of the thermal active restrained shrinkage ring test to study the early age behavior of massive concrete structures. *Engineering Structures*, 33(4):1390–1401, 2011.

[16] J. Mazars. Application de la mécanique de l'endommagement au comportement non linéaire et à la rupture du béton de structure. *Thèse de doctorat d'état de l'Université Paris VI*, 1984.

[17] J. Mazars. A description of micro-and macroscale damage of concrete structures. *Engineering Fracture Mechanics*, 25(5-6):729–737, 1986.

[18] C. de Sa, F. Benboudjema, M. Thiery, and J. Sicard. Analysis of microcracking induced by differential drying shrinkage. *Cement and Concrete Composites*, 30(10):947–956, 2008.

[19] F. Benboudjema, F. Meftah, and J-M. Torrenti. Interaction between drying, shrinkage, creep and cracking phenomena in concrete. *Engineering Structures*, 27(2):239–250, 2005.

[20] P. Grassl, H.S. Wong, and N.R. Buenfeld. Influence of aggregate size and volume fraction on shrinkage induced micro-cracking of concrete and mortar. *Cement and Concrete Research*, 40(1): 85–93, 2010.

[21] L. Jendele, V. Šmilauer, and J. Červenka. Multiscale hydro-thermo-mechanical model for early-age and mature concrete structures. *Advances in Engineering Software*, 72:134–146, 2014.

[22] T.T. Nguyen, D. Waldmann, and T.Q. Bui. Computational chemo-thermo-mechanical coupling phase-field model for complex fracture induced by early-age shrinkage and hydration heat in cement-based materials. *Computer Methods in Applied Mechanics and Engineering*, 348:1–28, 2019.

[23] M. Cervera, R. Faria, J. Oliver, and T. Prato. Numerical modelling of concrete curing, regarding hydration and temperature phenomena. *Computers & Structures*, 80(18-19):1511–1521, 2002.

[24] R. Lackner and H.A. Mang. Chemoplastic material model for the simulation of early-age cracking: From the constitutive law to numerical analyses of massive concrete structures. *Cement and Concrete Composites*, 26(5):551–562, 2004.

[25] V. Waller, L. d'Aloıa, F. Cussigh, and S. Lecrux. Using the maturity method in concrete cracking control at early ages. *Cement and Concrete Composites*, 26(5):589–599, 2004.

[26] R. Faria, M. Azenha, and J.A. Figueiras. Modelling of concrete at early ages: Application to an externally restrained slab. *Cement and Concrete Composites*, 28(6):572–585, 2006.

[27] M.N. Amin, J-S. Kim, Y. Lee, and J-K. Kim. Simulation of the thermal stress in mass concrete using a thermal stress measuring device. *Cement and Concrete Research*, 39(3):154–164, 2009.

[28] A.E. Idiart, C.M. López, and I. Carol. Modeling of drying shrinkage of concrete specimens at the meso-level. *Materials and Structures*, 44(2):415–435, 2011.

[29] G. De Schutter. Degree of hydration based kelvin model for the basic creep of early age concrete. *Materials and Structures*, 32(4):260, 1999.

[30] G.A. Francfort and J.J. Marigo. Revisiting brittle fracture as an energy minimization problem. *Journal of the Mechanics and Physics of Solids*, 46(8):1319–1342, 1998.

[31] B. Bourdin, G.A. Francfort, and J.J. Marigo. Numerical experiments in revisited brittle fracture. *Journal of the Mechanics and Physics of Solids*, 48(4):797–826, 2000.

[32] A. Karma, D. Kessler, and H. Levine. Phase-field model of mode III dynamic fracture. *Physical Review Letters*, 87(4):45501, 2001.

[33] B. Bourdin, G.A. Francfort, and J.J. Marigo. The variational approach to fracture. *Journal of Elasticity*, 91(1-3):5–148, 2008.

[34] C. Miehe, M. Hofacker, and F. Welschinger. A phase field model for rate-independent crack propagation: Robust algorithmic implementation based on operator splits. *Computer Methods in Applied Mechanics and Engineering*, 199:2765–2778, 2010.

[35] M.J. Borden, C.V. Verhoosel, M.A. Scott, T.J.R Hughes, and C.M. Landis. A phase-field description of dynamic brittle fracture. *Computer Methods in Applied Mechanics and Engineering*, 217:77–95, 2012.

[36] R. de Borst and C.V. Verhoosel. Gradient damage vs phase-field approaches for fracture: Similarities and differences. *Computer Methods in Applied Mechanics and Engineering*, 312:78–94, 2016.

[37] H. Amor, J.J. Marigo, and C. Maurini. Regularized formulation of the variational brittle fracture with unilateral contact: Numerical experiments. *Journal of the Mechanics and Physics of Solids*, 57(8):1209–1229, 2009.

[38] T.T. Nguyen, J. Yvonnet, M. Bornert, C. Chateau, K. Sab, R. Romani, and B. Le Roy. On the choice of parameters in the phase field method for simulating crack initiation with experimental validation. *International Journal of Fracture*, 197(2):213–226, 2016.

[39] J.A.T. de Freitas, P.T. Cuong, R. Faria, and M. Azenha. Modelling of cement hydration in concrete structures with hybrid finite elements. *Finite Elements in Analysis and Design*, 77:16–30, 2013.

[40] L. Stefan, F. Benboudjema, J-M. Torrenti, and B. Bissonnette. Prediction of elastic properties of cement pastes at early ages. *Computational Materials Science*, 47(3):775–784, 2010.

[41] S. Thelandersson. Modeling of combined thermal and mechanical action in concrete. *Journal of Engineering Mechanics*, 113(6):893–906, 1987.

[42] C. Miehe. Comparison of two algorithms for the computation of fourth-order isotropic tensor functions. *Computers & Structures*, 66(1):37–43, 1998.

[43] T.T. Nguyen, J. Yvonnet, Q-Z. Zhu, M. Bornert, and C. Chateau. A phase field method to simulate crack nucleation and propagation in strongly heterogeneous materials from direct imaging of their microstructure. *Engineering Fracture Mechanics*, 139:18–39, 2015.

[44] T.T. Nguyen, M. Weiler, and D. Waldmann. Experimental and numerical analysis of early age behavior in non-reinforced concrete. *Construction and Building Materials*, 210:499–513, 2019.

[45] T.T. Nguyen. *Modeling of complex microcracking in cement based materials by combining numerical simulations based on a phase-field method and experimental 3D imaging*. PhD thesis, Université Paris-Est, 2015.

[46] O. Bernard, F-J. Ulm, and E. Lemarchand. A multiscale micromechanics-hydration model for the early-age elastic properties of cement-based materials. *Cement and Concrete Research*, 33(9): 1293–1309, 2003.

[47] C. Pichler, R. Lackner, and H.A. Mang. A multiscale micromechanics model for the autogenous-shrinkage deformation of early-age cement-based materials. *Engineering Fracture Mechanics*, 74 (1-2):34–58, 2007.

[48] S. Liang, Y. Wei, and Z. Wu. Multiscale modeling elastic properties of cement-based materials considering imperfect interface effect. *Construction and Building Materials*, 154:567–579, 2017.

[49] Z. Bažant and S. Prasannan. Solidification theory for aging creep. *Cement and Concrete Research*, 18(6):923–932, 1988.

[50] Paul P. Acker et al. Micromechanical analysis of creep and shrinkage mechanisms. *Creep, Shrinkage and Durability Mechanics of Concrete and other quasi-brittle Materials, Cambridge, MA*, pages 15–25, 2001.

[51] C. Miehe, L-M. Schänzel, and H. Ulmer. Phase field modeling of fracture in multi-physics problems. part I. balance of crack surface and failure criteria for brittle crack propagation in thermo-elastic solids. *Computer Methods in Applied Mechanics and Engineering*, 294:449–485, 2015.

[52] J-Y. Wu and V.P. Nguyen. A length scale insensitive phase-field damage model for brittle fracture. *Journal of the Mechanics and Physics of Solids*, 119:20–42, 2018.